MNRAS **000**, 1–20 (2015) Preprint 1 March 2022 Compiled using MNRAS LATEX style file v3.0

The nuclear and integrated far-infrared emission of nearby Seyfert galaxies⋆

J. García-González,[1] A. Alonso-Herrero,[1,2] A. Hernán-Caballero,[1,3] M. Pereira-Santaella,[4] C. Ramos-Almeida,[5,6] J. A. Acosta Pulido,[5,6] T. Díaz-Santos,[7] P. Esquej,[8,9] O. González-Martín,[10] K. Ichikawa,[11] E. López-Rodríguez,[12,13] M. Povic,[14] P. F. Roche,[2] and M. Sánchez-Portal[8,9]

[1] *Instituto de Física de Cantabria, CSIC-UC, Avenida de los Castros s/n, 39005 Santander, Spain*
[2] *Department of Physics, University of Oxford, Oxford OX1 3RH, UK*
[3] *Departamento de Astrofísica y CC. de la Atmósfera, Facultad de CC. Físicas, Universidad Complutense de Madrid, E-28040 Madrid, Spain*
[4] *Centro de Astrobiología (CSIC/INTA), Ctra de Torrejón a Ajalvir, km 4, E-28850 Torrejón de Ardoz, Madrid, Spain*
[5] *Instituto de Astrofísica de Canarias, E-38205, La Laguna*
[6] *Departamento de Astrofísica, Universidad de La Laguna, E-38206 La Laguna*
[7] *Núcleo de Astronomía de la Facultad de Ingeniería, Universidad Diego Portales, Av. Ejército Libertador 441, Santiago, Chile*
[8] *European Space Astronomy Centre (ESAC)/ESA, P.O. Box 78, 28690 Villanueva de la Cañada, Madrid, Spain*
[9] *ISDEFE, Beatriz de Bobadilla 3, 28040 Madrid, Spain*
[10] *Centro de Radioastronomía y Astrofísica (IRyA-UNAM), 3-72 (Xangari), 8701 Morelia, Mexico*
[11] *National Astronomical Observatory of Japan, 2-21-1 Osawa, Mitaka, Tokyo 181-8588, Japan*
[12] *Department of Physics & Astronomy, University of Texas at San Antonio, One UTSA Circle, San Antonio, TX 78249, USA*
[13] *Department of Astronomy, University of Texas at Austin, 1 University Station C1400, Austin, TX 78712, USA*
[14] *Instituto de Astrofísica de Andalucía (IAA-CSIC), E-18008 Granada, Spain*

arXiv:1603.04235v1 [astro-ph.GA] 14 Mar 2016

Accepted XXX. Received YYY; in original form ZZZ

ABSTRACT

We present far-infrared (FIR) $70-500\,\mu$m imaging observations obtained with *Herschel*/PACS and SPIRE of 33 nearby (median distance of 30 Mpc) Seyfert galaxies from the Revised Shapley-Ames (RSA) catalogue. We obtain the FIR nuclear ($r = 1$ kpc and $r = 2$ kpc) and integrated spectral energy distributions (SEDs). We estimate the unresolved nuclear emission at 70 μm and we fit the nuclear and integrated FIR SEDs with a grey body model. We find that the integrated FIR emission of the RSA Seyferts in our sample is dominated by emission from the host galaxy, with dust properties similar to those of normal galaxies (non AGN). We use four criteria to select galaxies whose nuclear 70 μm emission has a significant AGN contribution: (1) elevated 70/160 μm flux ratios, (2)spatially resolved, high dust temperature gradient, (3) 70 μm excess emission with respect to the fit of the FIR SEDs with a grey body, and (4) excess of nuclear SFR obtained from 70 μm over SFR from mid-infrared indicators. 16 galaxies (48 per cent of the initial sample) satisfy at least one of these conditions, whereas 10 satisfy half or more. After careful examination of these, we select six *bona fide* candidates (18 per cent of the initial sample) and estimate that $\sim 40-70$ per cent of their nuclear ($r = 1-2$ kpc) 70 μm emission is contributed by dust heated by the AGN.

Key words: galaxies: active – infrared: galaxies

1 INTRODUCTION

Seyfert galaxies emit a large fraction of their bolometric emission in the far-infrared (FIR) range (Rieke 1978). This emission is due to dust grains that re-radiate the absorbed optical and ultraviolet photons emitted by the active galactic nucleus (AGN) as well as by stars in their host galax-

⋆ *Herschel* is an ESA space observatory with science instruments provided by European-led Principal Investigator consortia and with important participation from NASA.

© 2015 The Authors

ies. Rodríguez Espinosa, Rudy, & Jones (1987) studied the FIR emission of a sample of optically selected Seyfert galaxies using observations taken with the *Infrared Astronomical Satellite (IRAS)*. They found that the distribution of the integrated FIR luminosities and 60 μm to 100 μm colours of Seyfert and starburst galaxies were indistinguishable and concluded that most of the FIR emission of Seyfert galaxies must be due to star formation processes. Using *Infrared Space Observatory (ISO)* observations, Pérez García, Rodríguez Espinosa, & Santolaya Rey (1998) showed that the integrated FIR thermal emission of Seyferts can be modelled with a combination of three different components: warm, cold, and very cold dust. The warm component is due to dust heated by the AGN and/or circumnuclear star formation (T$\sim$ 150 K), the cold component comes from dust heated by stars in the disc of the galaxy (T$\sim$ 40 $-$ 50 K) and the very cold component arises from dust heated by the general interstellar radiation field of the galaxy (T$\sim$ 10$-$20 K). Spinoglio et al. (2002) also found using *ISO* imaging data that the integrated FIR emission of Seyfert galaxies is dominated by emission from the host galaxy.

Mushotzky et al. (2014) used FIR observations taken with the Photodetector Array Camera (PACS; Poglitsch et al. 2010) on board *Herschel* to study a sample of hard X-ray selected galaxies from the 58 month *Swift* Burst Alert Telescope (BAT) Active Galactic Nuclei catalogue. They found that $>$ 35 per cent and 20 per cent of the sources are point-like at 70 and 160 μm, respectively. Using the same sample, Meléndez et al. (2014) showed that the integrated FIR luminosity distributions of Seyfert 1 and Seyfert 2 galaxies are similar and their integrated $f_\nu(70\mu\mathrm{m})/f_\nu(160\mu\mathrm{m})$ ratios are indistinguishable from those of normal galaxies. Hatziminaoglou et al. (2010) studied 469 spectroscopically confirmed AGN. They used the Spectral and Photometric Imaging REceiver (SPIRE; Griffin et al. 2010) data and showed that the FIR emission of Seyfert 1 and Seyfert 2 galaxies is identical to that of star forming galaxies. The AGN contributes very little to the integrated FIR emission and its contribution becomes important at wavelengths shorter than 70 μm, where the torus starts playing an important role.

According to the unified model of AGN (Antonucci 1993), there is a dusty torus surrounding the accreting supermassive black hole. Dusty torus models where the dust is distributed both homogeneously (e.g., Fritz, Franceschini, & Hatziminaoglou 2006) or in a clumpy configuration (see e.g., Nenkova et al. 2008; Hönig & Kishimoto 2010) predict emission in the FIR, although the torus emission peaks in the mid-infrared (MIR) spectral range. Based on studies of individual Seyfert galaxies using *Herschel* observations, the contribution of the dust heated by the AGN to the total FIR emission varies from galaxy to galaxy. For example, Alonso-Herrero et al. (2012) found that in NGC 1365 the AGN is the brightest source in the MIR but does not dominate in the FIR. Using the Nenkova et al. (2008) torus models they quantified the AGN emission at 70 μm and determined that the AGN only contributes at most 1 per cent within the central 5.4 kpc. For NGC 2992, García-Bernete et al. (2015) showed that the AGN dominates the emission between 15 and 30 μm, but its contribution decreases rapidly for wavelengths $>$ 30 μm. Ramos Almeida et al. (2011) studied NGC 3081 and found that the FIR nuclear luminosity within a radius of $\leq$ 0.85 kpc was well reproduced with the Nenkova et al. (2008) clumpy torus models and concluded that the AGN dominates the FIR nuclear luminosity of this galaxy. There are however no statistical studies of the AGN contribution in the FIR, so it is important to find a method to determine if the AGN dominates in the FIR for large samples of galaxies. Mullaney et al. (2011) studied the infrared emission of a sample of local X-ray selected AGN with little evidence of host galaxy contamination in their MIR *Spitzer*/IRS spectra. They found that at least 3 of the 11 AGN in their sample are AGN dominated even at 60 μm.

In this work we study the FIR (70$-$500 μm) emission of a sample of 33 nearby (median distance of 30 Mpc) Seyfert galaxies drawn from the Revised Shapley-Ames catalogue (RSA; Sandage & Tammann 1987) using *Herschel* imaging observations taken with PACS and SPIRE. The main goal is to disentangle the FIR emission of these Seyfert galaxies due to dust heated by the AGN from that due to dust heated by star formation. In particular, we take advantage of the *Herschel* angular resolution of 5.6 arcsec at 70 μm, which provides a median physical resolution of 0.8 kpc for our sample of galaxies. This allows us to study the nuclear (radii of r = 1 kpc and r = 2 kpc) and integrated FIR emission of Seyfert galaxies. The paper is organized as follows. In Section 2 we present our sample selection and the comparison with the entire RSA sample. In Section 3 we describe the data reduction and derive the aperture photometry. Section 4 presents our results, such as the unresolved 70 μm emission, the FIR colours, the grey body fitting and the nuclear and extranuclear star formation rates (SFR). In Section 5 we put forward a number of criteria to identify those Seyfert galaxies in our sample whose 70 μm emission is mostly due to dust heated by the AGN and discuss the *bona fide* candidates. The conclusions are presented in Section 6. Throughout this work we use a cosmology with $H_0 = 73\,\mathrm{km\,s^{-1}\ Mpc^{-1}}$, $\Omega_m = 0.27$ and $\Omega_\Lambda = 0.73$.

2 THE SAMPLE

We selected a sample of 33 nearby (distances $D_L < 70$ Mpc, Table 1) Seyfert galaxies (see Maiolino & Rieke 1995) from the RSA catalogue (Sandage & Tammann 1987) with *Herschel*/PACS imaging observations in at least two bands and SPIRE imaging observations from our own programs and from the archive[1] (see Table 3). We imposed the distance criterion so we could obtain at least one nuclear (radii of r = 1 kpc and/or r = 2 kpc) FIR measurement at 70 μm. We also required Seyfert galaxies with existing high angular resolution (0.3$-$0.4″) MIR spectroscopy (Hönig et al. 2010; González-Martín et al. 2013; Esquej et al. 2014; Alonso-Herrero et al. 2016) obtained on 8 $-$ 10 m class telescopes (T-ReCS, CanariCam and VISIR instruments). We used the spectra published in these references instead of reducing the archival data. These observations allow us to determine whether they have star formation activity on typical physical scales of 50 $-$ 60 pc, which is necessary when trying to determine what galaxies in our sample have AGN-dominated FIR emission. 23 of these galaxies also have estimates of the

[1] http://www.cosmos.esa.int/web/herschel/science-archive

nuclear and integrated SFR from mid-IR *Spitzer*/IRS spectroscopy taken from Diamond-Stanic & Rieke (2012) (hereafter DSR2012).

In Table 1 we list the properties of the Seyfert galaxies in our sample including their luminosity distance, optical apparent magnitude (B_T), morphological type, and the optical activity type (15 Sy 1 galaxies and 18 Sy 2 galaxies). We consider as Sy 1 the 1.5 and 1.9 Seyfert galaxies.

We obtained the *Spitzer*/IRS SL+LL spectra from the Cornell Atlas of Spitzer/IRS Sources version 7 (CASSIS, Lebouteiller et al. 2011, 2015). The stitching of the different spectral orders has been made as described in Hernán-Caballero et al. (2016). We also provide in Table 1 the equivalent width (EW) of the 6.2 and 11.3 μm PAH features measured from *Spitzer*/IRS short-low (SL) spectra, except for NGC 1068 which was from a short-high (SH) spectrum (see Esquej et al. 2014). We measured the EW of the PAH features following the method described by Hernán-Caballero & Hatziminaoglou (2011). Finally, we give the AGN bolometric luminosity, and the nuclear ($r = 1$ kpc) and extranuclear ($r > 1$ kpc) SFRs taken from DSR2012. For those RSA Seyferts not in that work we take the AGN bolometric luminosities from Mason et al. (2012) and Esquej et al. (2014).

Table 1. Galaxy sample.

Number	Name	D_L (Mpc)	B_T[1] (mag)	Morphological[2] type	Activity type	EW of 6.2μm PAH (μm)	EW of 11.3μm PAH (μm)	log $L_{bol,AGN}$[6] ($erg\ s^{-1}$)	SFR (r=1kpc)[6] ($M_\odot yr^{-1}$)	SFR (r>1kpc)[6] ($M_\odot yr^{-1}$)	Ref. Activity type
1	ESO 323-G077	60.2	13.58	(R)SAB0^0(rs)	Sy 1.2	0.049±0.005	0.126±0.005	43.9[8]			3
2	IC 5063	49.9	13.22	SA0^+(s)?	Sy 2	<0.018	0.011±0.004	44.0[8]			10
3	Mrk 1066	49.0	13.64	(R)SB0^+(s)	Sy 2	0.544±0.007	0.591±0.005				4
4	NGC 1068	14.4	9.61	(R)SA(rs)b	Sy 2			44.3[8]			5
5	NGC 1320	35.5	13.32	Sa? edge-on	Sy 2						3
6	NGC 1365	21.5	10.21	SB(s)b	Sy 1.8	0.258±0.004	0.314±0.002	44.3	4.80	8.40	3
7	NGC 1386	10.6	12.00	SB0^+(s)	Sy 2	<0.019	0.072±0.005	43.5	0.05		11
8	NGC 1808	12.3	10.76[2]	(R)SAB(s)a	Sy 2	1.078±0.006	1.013±0.003	41.2[8]			7
9	NGC 2110	32.4	14.00	SAB0^-	Sy 2	0.014±0.007	0.051±0.005	43.7[8]			12
10	NGC 2273	28.7	12.55	SB(r)a?	Sy 2	0.273±0.006	0.383±0.007	43.6	0.76		4
11	NGC 2992	34.1	12.80	Sa pec	Sy 1.9	0.295±0.008	0.328±0.017	44.7	0.77	0.54	1
12	NGC 3081	34.2	12.68	(R)SAB0/a(r)	Sy 2	0.022±0.012	0.046±0.005	44.6	0.15	0.31	13
13	NGC 3227	20.6	11.55	SAB(s)a pec	Sy 1.5	0.215±0.006	0.359±0.007	44.0	0.48	0.21	3
14	NGC 3281	44.7	12.62	SA(s)ab pec?	Sy 2	0.013±0.008	0.010±0.011	45.0	0.87		3
15	NGC 3783	36.1	12.89	(R')SB(r)ab	Sy 1.5	0.001±0.005	0.013±0.009	44.2	0.05		3
16	NGC 4051	12.9	10.93	SAB(rs)bc	Sy 1.5	0.089±0.004	0.114±0.003	43.5	0.13	0.88	1
17	NGC 4151	20.3	11.13	(R')SAB(rs)ab?	Sy 1.5	0.005±0.003	0.013±0.003	44.5	0.06		3
18	NGC 4253	61.3	13.30	(R')SB(s)a?	Sy 1.5	0.087±0.005	0.083±0.005				1
19	NGC 4258	7.98	8.95	SAB(s)bc	Sy 1.9	0.034±0.013	0.067±0.009	42.2	0.05	0.39	1
20	NGC 4388	17.0	11.83	SA(s)b? edge-on	Sy 2	0.072±0.005	0.140±0.003	44.4	0.21	0.24	14
21	NGC 4507	59.6	12.81	(R')SAB(rs)b	Sy 2	0.019±0.006	0.049±0.003	44.6	0.99		10
22	NGC 4579	17.0	10.56	SAB(rs)b	Sy 1.9			42.4[9]	0.05	0.47	1
23	NGC 4594	12.7	9.28	SA(s)a edge-on	Sy 1.9			42.5	0.03	0.66	1
24	NGC 4725	27.0	10.11[2]	SAB(r)ab pec	Sy 2			41.9	0.01	0.34	3
25	NGC 5135	57.7	12.94	SB(s)ab	Sy 2	0.742±0.009	0.777±0.007	44.9	6.10	3.60	3
26	NGC 5347	40.2	13.40	(R')SB(rs)ab	Sy 2	0.046±0.001	0.059±0.005	43.5[8]			3
27	NGC 5506	30.0	12.79	Sa pec edge-on	Sy 1.9	0.012±0.004	0.055±0.003	44.8	0.58		1
28	NGC 7130	68.7	12.98[2]	Sa pec	Sy 1.9	0.416±0.011	0.434±0.008	44.3	4.30	6.70	3
29	NGC 7172	37.6	12.85	Sa pec edge-on	Sy 2	0.052±0.006	0.205±0.009	44.2	0.79	0.68	3
30	NGC 7213	24.9	11.18	SA(s)a?	Sy 1.5	<0.025	0.059±0.006	43.1[8]	0.04	0.39	1
31	NGC 7465	28.4	13.31	(R')SB0^0?(s)	Sy 2						15
32	NGC 7479	32.4	11.70	SB(s)c	Sy 1.9		0.008±0.008	43.2	0.32	1.70	3
33	NGC 7582	22.0	11.46	(R')SB(s)ab	Sy 2	0.508±0.033	0.703±0.011	44.5	2.10	1.90	1

[1] from Maiolino & Rieke (1995); [2] NED Homogenized from de Vaucouleurs et al. (1991) ;[3] from Véron-Cetty & Véron (2006); [4] from Contini, Considere & Davoust (1998); [5] from Osterbrock & Martel (1993); [6] from Diamond-Stanic & Rieke (2012); [7] from Brightman & Nandra (2011); [8] from Esquej et al. (2014); [9] from Mason et al. (2012); [10] from Kewley et al. (2001); [11] from Reunanen, Kotilainen, & Prieto (2002); [12] from Bradt et al. (1978); [13] from Phillips, Charles, & Baldwin (1983); [14] from Trippe et al. (2010); [15] from Malizia et al. (2012)

2.1 Sample comparison

Since the RSA sample is selected based on the galaxy optical apparent magnitude, we used the B_T values from Maiolino & Rieke (1995) to determine if our galaxy selection is representative of the entire RSA sample of Seyfert galaxies. Their sample contains 91 relatively nearby Seyfert galaxies with B_T <13.31 and have 30 galaxies in common with our sample. The top left panel of Fig. 1 shows the B_T distribution for the two samples. The 91 galaxies in Maiolino & Rieke (1995) are shown in red and the 30 of 33 galaxies in our sample are shown in blue. Inspection of Fig. 1 and a Kolmogorov-Smirnov (K-S) test show that our sample is not significantly different from the RSA sample in terms of B_T (p-value= 0.92).

We also compared the luminosity distance of our sample those of the 84 galaxies in DSR2012. They selected Seyfert galaxies in the RSA sample with *Spitzer*/IRS observations of the 11.3 μm PAH feature. We used, as DSR2012, the luminosity distance obtained from the Nasa Extragalactic Database (NED[2]) using the corrected redshift to the reference frame defined by the Virgo cluster, the Great Attractor and the Shapley supercluster. The right top panel of Fig. 1 shows the luminosity distance distributions for the 84 galaxies in DSR2012 and the 33 galaxies of our sample (median luminosity distance of 30 Mpc). There are 10 Seyfert galaxies in our sample not in DSR2012 selection but in the RSA catalogue. Again, from Fig. 1 and a K-S test (p=0.87) our sample is not statistically significantly different in terms of the luminosity distance.

Since the main goal of this paper is to select galaxies with evidence of strong contribution of the AGN at 70 μm emission, in Section 4.4 we will compare the nuclear SFR from MIR spectroscopy and *Herschel* 70 μm photometry. We therefore compared the nuclear SFR values obtained by DSR2012 for all their sample and the 23 galaxies in common with our sample. The bottom left panel of Fig. 1 shows the nuclear SFR distribution in DSR2012 and our sample with DSR2012 SFR values (median of 0.32 $M_{\odot}yr^{-1}$). A K-S test shows that both samples are not statistically different in terms of the SFR ($p = 0.42$).

We finally compared the AGN bolometric luminosity distributions for the galaxies in DSR2012 and our galaxies with their values. This comparison is shown in the right bottom panel of Fig. 1. Clearly, our sample only includes the most luminous AGN $L_{bol} > 10^{43}$ erg s^{-1} when compared to the DSR2012 RSA sample. We find a p value for the K-S test of $p = 0.03$ when comparing with the galaxies in common and $p = 0.05$ when comparing with all our sample. This is because in general low-luminosity AGN are not bright in the mid-IR and thus few meet our requirement of having high angular resolution MIR spectroscopy obtained from the ground (see Alonso-Herrero et al. 2016). Even in the mid-infrared the low-luminosity AGN do not dominate the emission at least in the 40 per cent of the cases (González-Martín et al. 2015). Table 2 summarizes the statistics of the above comparisons.

3 HERSCHEL OBSERVATIONS

In this section we describe the process of obtaining the PACS and SPIRE images from the *Herschel* archive, the data reduction and the aperture photometry.

The PACS instrument has three bands referred to as blue, green, and red with central wavelengths of 70, 100, and 160 μm, respectively. The nominal angular resolutions are 5.6, 6.8, and 11.3 arcsec (FWHM). The red band can be combined with the blue or the green band, for simultaneous observations.

The SPIRE instrument has three bands centred at 250, 350, and 500 μm, with beam sizes of 18.1, 25.2, and 36.9 arcsec (FWHM), respectively. The three bands are observed simultaneously.

3.1 Data reduction

We compiled all the PACS and SPIRE images for our 33 galaxies using the Herschel Science Data Archive (HSA)[3]. First, we processed the raw level 1 data with the Herschel interactive pipeline environment software (HIPE) version 13 (Ott 2010) to obtain the flux calibrated timelines of each bolometer. The standard HIPE pipeline corrects for instrumental effects and attaches pointing information to the timelines. Then, we combined these timelines using Scanamorphos version 24 (Roussel 2013). Scanamorphos subtracts low-frequency noise (thermal and non-thermal), masks high-frequency glitches of the data, and projects the timelines into a spatial grid. For the spatial grids, we selected a pixel size of FWHM/4 for each band. These values provide a good compromise between angular resolution and sampling (> 10 samples per pixel). We discarded mosaics at 100 μm where the galaxy reaches the edge of the image only in these band because we could not obtain reliable measurements of the background and could not obtain the integrated flux in the same aperture as the other bands. Only 22 of the 33 galaxies (67 per cent of the sample) have observations at 100 μm after discarding these images. The list of all the observations used can be found in Table 3. Fig. 2 shows an example of the mosaics of one galaxy in our sample observed in all PACS and SPIRE bands. The mosaics for the rest of the sample are available online. The number of images used for each band is given in Table 4.

3.2 Aperture photometry

Circular aperture photometry of the galaxies was carried out using HIPE version 13. For every galaxy and every band we performed the photometry for radii of 1 kpc, and 2 kpc, as well as for the total galaxy. To determine the size in arcsec corresponding to 1 kpc and 2 kpc we took into account the luminosity distance of each galaxy. The aperture corresponding to the total galaxy was determined by visual inspection of the radial profiles in all the bands. In Table 7 we list the apertures used for the total photometry. We imposed that the aperture had to be the same for all the bands. In some galaxies, part of the galaxy seen in the SPIRE bands is outside the aperture used for the photometry. To avoid

[2] http://ned.ipac.caltech.edu/

[3] http://www.cosmos.esa.int/web/herschel/science-archive

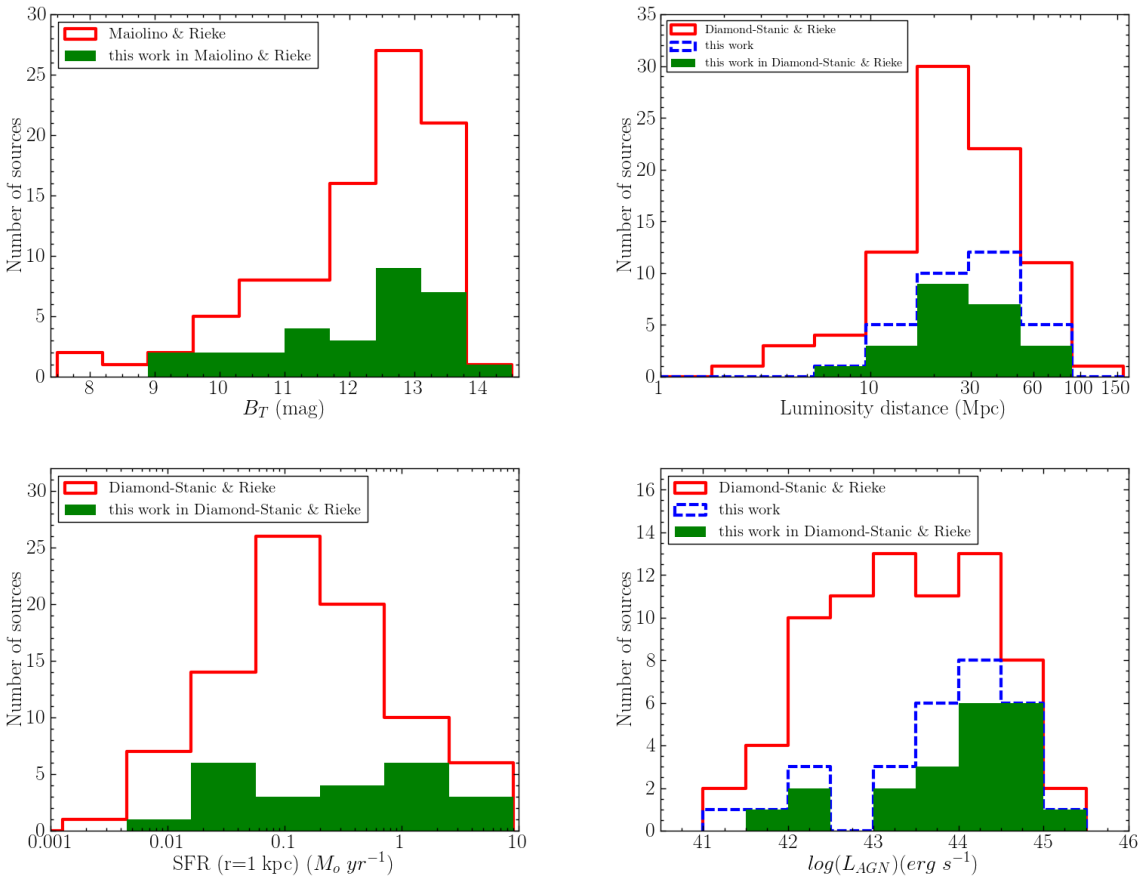

Figure 1. Sample comparison. Top left panel: Distribution of the optical apparent magnitude, B_T, for the RSA galaxies in Maiolino & Rieke (1995) (91 galaxies, in red) and our sample (30 galaxies, in green). Top right panel: Distribution of the luminosity distance for the galaxies in DSR2012 (84 galaxies, in red) and our sample (33 galaxies, in dashed blue). There are 10 galaxies in our sample not included in the DSR2012 sample. The galaxies in common between DSR2012 sample and our sample are shown in green. Bottom left panel: Distribution of the nuclear SFR (r=1kpc) for the galaxies in DSR2012 (84 galaxies, in red) and our sample with DSR2012 SFR values (23 galaxies, in green). Bottom right panel: Distribution of the AGN bolometric luminosity for the galaxies in DSR2012 (74 galaxies, in red), our sample (29 galaxies, in dashed blue) and our sample with DSR2012 values (21 galaxies, in blue).

Table 2. Summary of the statistical properties of our sample and comparison samples.

	RSA sample				This work			
Quantity	Number	Mean	σ	Median	Number	Mean	σ	Median
B_T [1]	91	12.08	1.32	12.55	30	12.10	1.34	12.68
Luminosity distance (Mpc) [2]	84	30.5	21.1	24.4	33 (23)*	32.2 (29.5)*	16.4 (15.6)*	30.0 (27.0)*
SFR (r=1kpc) ($M_\odot yr^{-1}$) [2]	84	0.67	1.42	0.15	23	1.03	1.66	0.32
log L_{AGN} (erg s^{-1}) [2]	74	43.4	1.0	43.4	29 (21)*	43.8 (44.0)*	1.0 (0.9)*	44.0 (44.3)*

[1] From Maiolino & Rieke (1995)
[2] From DSR2012
∗ In parenthesis are galaxies in our sample in common with DSR2012.

errors in the photometry due to the small size of the aperture, we only consider fluxes from nuclear apertures with a diameter higher than 1.5 times the angular resolution of each band. The photometric error of each image is determined by placing six apertures on the background around the source and measuring the standard deviation per pixel of the background within these apertures. The error in the flux was then computed by multiplying the standard deviation per pixel by the number of pixels of the aperture.

We measured the FWHM for each galaxy at each band using Moffat with the Image Reduction and Analysis Facility (IRAF[4]). We list in Table 4 the measured FWHM in all

[4] IRAF is distributed by the National Optical Astronomy Observatory, which is operated by the Association of Universities for

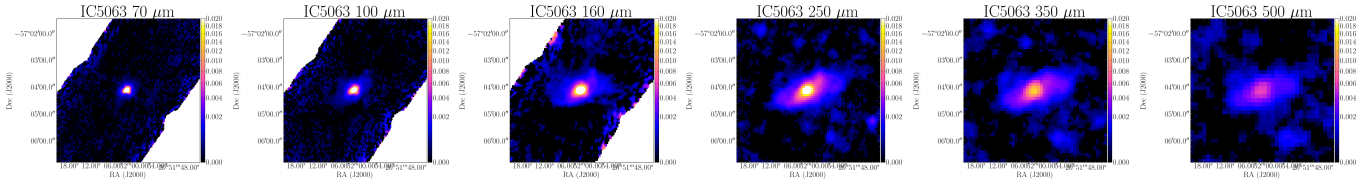

Figure 2. Example of the mosaics of IC 5063 in the PACS 70, 100, and 160 μm bands (the three most left panels, left to right), and in the SPIRE 250, 350, and 500 μm bands (the three most right panels from left to right). The images are shown in a square root scale. The rest of the galaxies are available in the online version.

Table 3. *Herschel*/PACS and SPIRE observing programs. The full table is available in the online version.

Galaxy	Observation ID	Instrument	Wavelengths (μm)	PI
ESO 323-G077	1342236922	PACS	70, 160	Mushotzky R.
ESO 323-G077	1342236923	PACS	70, 160	Mushotzky R.
ESO 323-G077	1342236202	SPIRE	250, 350, 500	Mushotzky R.
IC 5063	1342216469	PACS	70, 160	Sánchez-Portal M.
IC 5063	1342216470	PACS	70, 160	Sánchez-Portal M.
IC 5063	1342216471	PACS	100, 160	Sánchez-Portal M.
IC 5063	1342216472	PACS	100, 160	Sánchez-Portal M.
IC 5063	1342206208	SPIRE	250, 350, 500	Sánchez-Portal M.

Table 4. FWHMs measured in the six FIR bands.

	FWHM ($''$)						Number of images			FWHM (kpc)
Galaxy	70 μm	100 μm	160 μm	250 μm	350 μm	500 μm	70 μm	100 μm	160 μm	70 μm
ESO 323-G077	6.7		12.4	19.2	25.4	36.7	2	-	2	1.9
IC 5063	6.0	7.8	13.1	22.6	33.6	51.9	2	2	4	1.4
Mrk 1066	5.9	7.2	11.8	19.5	25.9	38.4	2	2	4	1.4
NGC 1068	6.6		21.3	36.1	39.9	48.0	2	-	2	0.5
NGC 1320	6.1	8.4	14.7	22.2	28.5	41.2	2	2	4	1.0
NGC 1365	10.3	11.9	17.4	23.7	29.9	39.9	2	2	4	1.1
NGC 1386	6.1	8.0	14.5	23.8	30.4	39.8	2	2	4	0.3
NGC 1808	9.4	11.2	15.3	21.3	28.3	39.8	2	2	4	0.6
NGC 2110	6.6	8.3	13.2	20.6	27.2	46.0	2	2	4	1.0
NGC 2273	6.1	7.6	12.2	20.4	27.9	40.5	2	2	4	0.8
NGC 2992	7.9	9.5	14.2	21.1	28.6	39.9	2	2	4	1.3
NGC 3081	6.2	8.1	13.3	22.9	37.6	65.1	2	2	4	1.0
NGC 3227	6.3		12.7	22.4	31.9	46.4	2	-	4	0.6
NGC 3281	5.8	7.3	11.9	19.5	26.8	39.4	2	2	4	1.3
NGC 3783	5.7	7.4	22.0	52.7	57.8	60.8	2	2	4	1.0
NGC 4051	6.0		14.7	31.2	49.3	183.6	2	-	4	0.4
NGC 4151	5.9		13.7	31.3	44.5	141.7	2	-	4	0.6
NGC 4253	5.8	7.2	11.9	19.7	28.3	66.0	2	2	4	1.7
NGC 4258	49.9	71.4	71.3	90.8	73.3	97.7	3	1	4	1.9
NGC 4388	6.9		15.7	26.6	36.4	51.8	2	-	2	0.6
NGC 4507	5.7		12.8	28.5	44.2	58.1	2	-	2	1.6
NGC 4579	7.0	9.3	110.6	27.4	39.6	138.5	2	2	4	0.6
NGC 4594	6.9	11.8	69.7	57.9	43.8	47.0	2	2	4	0.4
NGC 4725	10.7	24.1	22.6	73.0	87.6	308.8	2	2	4	1.4
NGC 5135	6.8	8.1	12.3	19.7	26.3	40.6	2	2	4	1.9
NGC 5347	5.6	7.4	12.7	25.6	43.9	66.3	2	2	4	1.1
NGC 5506	6.0	7.4	12.0	20.2	27.4	42.8	2	2	4	0.9
NGC 7130	5.8		12.9	20.8	27.6	39.7	2	-	2	1.9
NGC 7172	7.1		13.4	20.8	27.3	41.2	2	-	2	1.3
NGC 7213	6.5		20.1	53.0	61.4	60.3	2	-	2	0.8
NGC 7465	7.3	9.2	14.1	22.1	30.0	47.2	2	4	6	1.0
NGC 7479	5.6	7.3	12.3	21.6	32.3	47.9	2	2	4	0.9
NGC 7582	6.6		12.3	19.8	26.7	42.6	2	-	4	0.7

Notes.— All the galaxies have one image at the SPIRE bands except NGC 4258 and NGC 7465, which have two images.

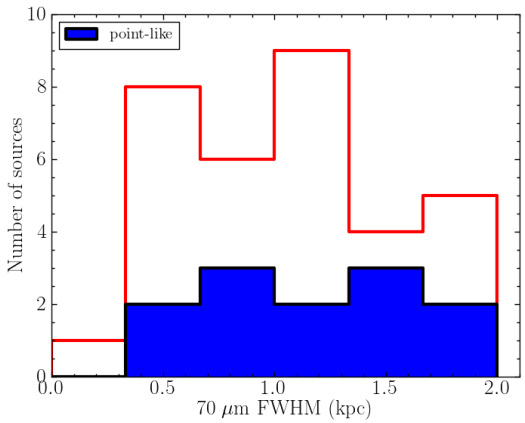

Figure 3. Distribution of the measured FWHM at 70 μm in kpc for our sample (open histogram). The filled histograms are those nuclei which appear unresolved at this wavelength, that is, with FWHM<6 arcsec.

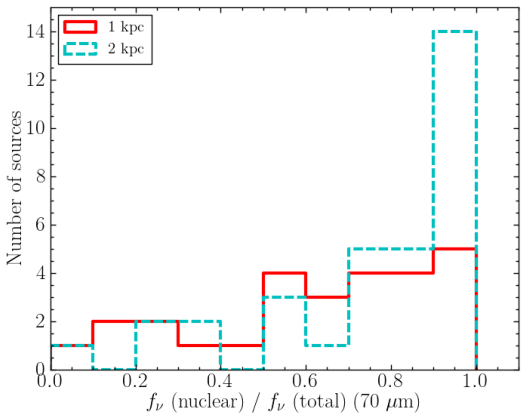

Figure 4. Distribution of the ratio between nuclear and total flux at 70 μm for $r = 1$ kpc for (27 galaxies, in red) and $r = 2$ kpc (33 galaxies, in dashed cyan).

six *Herschel* bands. We then applied an aperture correction using HIPE to the fluxes of those galaxies that are point sources and quasi point sources. We did not apply an aperture correction to the extended sources. We consider that a source is quasi point-like at one particular band (although it may have extended emission) when the measured FWHM (see Table 4) is less than the FWHM of the instrument plus the number of arcseconds in one pixel. For a typical galaxy in our sample at 30 Mpc, the aperture correction at 70 μm is 1.48 and 1.22 for photometry radio of 1 and 2 kpc, respectively. For sources that are quasi point-like the unresolved fluxes are probably slightly overestimated, as we shall see in Section 4.1. This is due to the instrumental Point Spread Function (PSF) that causes that a fraction of the external emission of the aperture to be observed in the inner region. However, although this correction cannot be calculated, it should be within the flux error and it does not modify our results.

To obtain the final error of the fluxes we added in quadrature the photometric calibration uncertainties (10 per cent) to the error calculated above. In Tables 5, 6 and 7 we provide the fluxes for all galaxies and all bands for $r = 1$ kpc, $r = 2$ kpc, and the total galaxy. We also list, for every galaxy, the size in arcsec for the aperture used. As can be seen from this table, the photometric calibration uncertainty dominates in most cases.

4 RESULTS

In this Section we analyse the FIR properties of our sample, such as, the unresolved 70 μm emission, the FIR colour distributions, the results from fitting the data to a grey body and the SFR nuclear and extranuclear obtained from the 70 μm data.

Research in Astronomy (AURA), Ibc., under cooperative agreement with the National Science Foundation.

4.1 Unresolved 70 μm emission

Of the 33 galaxies in our sample, 12 nuclei (31 per cent) appear point-like at 70 μm, i.e., have FWHM < 6 arcsec (see Table 4). As can be seen from Fig. 3, the 70 μm emission for those nuclei seen as point sources originates in regions with sizes (diameters) of less than $\sim 0.5 - 2$ kpc, with a median size of 1.3 kpc. These values are, however, comparable to those nuclei in our sample that appear clearly extended at 70 μm (median size of 1.0 kpc). The fraction of RSA Seyfert galaxies with unresolved emission is similar to that of the *Swift*/BAT hard X-ray selected AGN sample of Mushotzky et al. (2014). They found that >35 per cent of their sources are point-like at 70 μm with typical sizes at 70 μm of 2 kpc. However, the *Swift*/BAT AGN sample is on average at $z \sim 0.025$, compared to the average $z = 0.007$ of our sample. Therefore, it is likely that the difference in redshifts between our sample and the *Swift*/BAT sample explains the different physical sizes for the 70μm emitting nuclear region.

To study further the unresolved 70 μm emission we estimated the contribution of the nuclear region to the total flux at 70 μm, as is shown in Fig. 4. The median values of the nuclear contributions to the total flux are 0.68 and 0.86 for $r = 1$ kpc and $r = 2$ kpc, respectively (see Table 8).

Of the 27 galaxies with measurements of the nuclear flux in $r = 1$ kpc at 70 μm, 20 (74 per cent) have a nuclear 1 kpc contribution to the total flux greater than 50 per cent. Of the 33 galaxies with nuclear fluxes within $r = 2$ kpc at 70 μm, 28 (85 per cent) have a nuclear $r = 2$ kpc contribution greater than 50 per cent. The values obtained for 1 kpc and 2 kpc are similar because 88 per cent of the galaxies required an aperture correction for the fluxes. Our results are in agreement with Mushotzky et al. (2014). They found that 92.5 per cent (274 out of 296 galaxies) of their sample had a point source contribution greater than 50 per cent of the total flux at 70 μm. They found a slightly higher percentage because they performed the photometry with an aperture of 6 arcsec for the PACS 70 μm images for all the galaxies, independently of their distance. As their galaxies are more distant than our sample, then the regions for their nuclear photometry are larger than our $r = 1$ kpc and $r = 2$ kpc

Table 5. Aperture photometry for r = 1 kpc. The full table is available in the online version.

Galaxy	radius (arcsec)	Flux 70μm (Jy)	Flux 100μm (Jy)	Flux 160μm (Jy)	Flux 250μm (Jy)	Flux 350μm (Jy)	Flux 500μm (Jy)
ESO 323-G077	3.43						
IC 5063	4.13						
Mrk 1066	4.21	12±1					
NGC 1068	14.32	164±16		88±9	28±3		
NGC 1320	5.81	1.8±0.2	2.0±0.2				

Table 6. Aperture photometry for r = 2 kpc. The full table is available in the online version.

Galaxy	radius (arcsec)	Flux 70μm (Jy)	Flux 100μm (Jy)	Flux 160μm (Jy)	Flux 250μm (Jy)	Flux 350μm (Jy)	Flux 500μm (Jy)
ESO 323-G077	6.85	6.9±0.7					
IC 5063	8.27	4.5±0.5	3.6±0.4				
Mrk 1066	8.42	12±1	12±1				
NGC 1068	28.65	253±25		186±19	65±7	23±2	8.0±0.8
NGC 1320	11.62	2.2±0.2	2.8±0.3	2.3±0.2			

Table 7. Integrated photometry. The full table is available in the online version.

Galaxy	radius (arcsec)	Flux 70μm (Jy)	Flux 100μm (Jy)	Flux 160μm (Jy)	Flux 250μm (Jy)	Flux 350μm (Jy)	Flux 500μm (Jy)
ESO 323-G077	50	6.8±0.8		7.1±0.8	3.2±0.3	1.3±0.1	0.43±0.04
IC 5063	60	4.7±0.5	4.6±0.5	3.7±0.4	2.1±0.2	0.9±0.1	0.30±0.04
Mrk 1066	50	12±1	13±1	8.5±0.9	3.0±0.3	1.1±0.1	0.33±0.04
NGC 1068	230	292±30		299±30	117±12	45±5	15±2
NGC 1320	50	2.4±0.3	3.4±0.4	3.0±0.4	1.5±0.2	0.58±0.07	0.20± 0.03

Table 8. Contribution of the nuclear regions of r = 1 kpc and 2 kpc to the total flux at 70 μm in RSA Seyferts

Quantity	Number	Mean	σ	Median
f_ν(r=1kpc)/f_ν(total)	27	0.63	0.28	0.68
f_ν(r=2kpc)/f_ν(total)	33	0.76	0.26	0.86

nuclear regions. We note that Mushotzky et al. (2014) also performed an aperture correction to the fluxes.

4.2 FIR colours

We first start by discussing the $f_\nu(70\ \mu\text{m})/f_\nu(160\ \mu\text{m})$ flux ratio since we can still obtain nuclear values for a significant fraction of galaxies in our sample. It provides information about the peak of the galaxy spectral energy distribution (SED) and is a proxy for the dust temperature (Skibba et al. 2011; Meléndez et al. 2014). Figure 5 shows the distributions of this ratio for $r = 1$ kpc and $r = 2$ kpc, and for the entire galaxy. As can be seen from this figure (see Table 9 for the statistical information), the flux ratios for the nuclear regions tend to be higher than those measured for the entire galaxies. This is in good agreement with the decreasing $f_\nu(70\ \mu\text{m})/f_\nu(160\ \mu\text{m})$ flux ratios with galactocentric radius found for M81 and M83 (Bendo et al. 2012). These authors suggested that this ratio tends to be more strongly influenced by star forming regions than other FIR ratios involving longer wavelengths. Therefore, the higher nuclear ratios in our sample could be due to higher star formation activity but also to higher dust temperature due to AGN heating (see further discussion in Section 5).

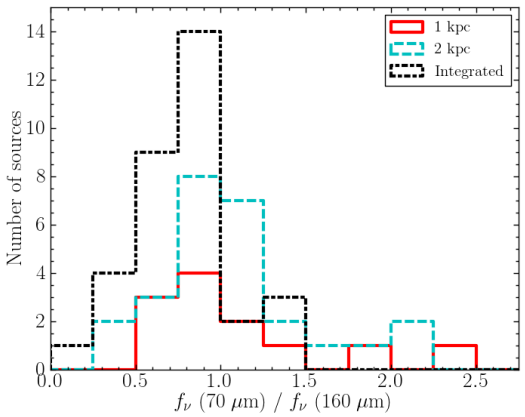

Figure 5. Distribution of the $f_\nu(70\ \mu\text{m})/f_\nu(160\ \mu\text{m})$ flux ratios within $r = 1$ kpc (12 galaxies, solid red line), within $r = 2$ kpc (26 galaxies, dashed cyan line), and for the integrated galaxy (33 galaxies, dash-dot black line) for the RSA Seyferts.

For the *Swift*/BAT AGN sample, Meléndez et al. (2014) measured a mean integrated $f_\nu(70\ \mu\text{m})/f_\nu(160\ \mu\text{m})$ flux ratio of 0.81 ± 0.43 for Seyfert 1s and 0.77 ± 0.47 for Seyfert 2s.

Table 9. Comparison of the observed $f_\nu(70\ \mu m)/f_\nu(160\ \mu m)$ flux ratios for different samples

Region	Number	Mean	σ	Median
RSA Seyferts				
$r = 1$ kpc	12	1.13	0.52	0.98
$r = 2$ kpc	26	1.08	0.44	1.01
Integrated	33	0.78	0.30	0.80
Swift/BAT AGN				
Integrated	258	0.79	0.44	0.68
PG quasars				
Integrated	68	1.41	0.87	1.25
KINGFISH galaxies				
Integrated normal	29	0.75	0.45	0.66
Integrated AGN	31	0.51	0.27	0.43
Integrated all	60	0.63	0.39	0.50

These are fundamentally the same as for our sample of optically selected AGN. Meléndez et al. (2014) also compared their observed colours with predictions from three different torus models and found that the torus models cannot produce $f_\nu(70\ \mu m)/f_\nu(160\ \mu m)$ ratios of less than unity. This suggests that the 70 μm and 160 μm integrated emission is dominated by the host galaxy.

Meléndez et al. (2014) also compared the *Swift*/BAT AGN FIR colour distribution with the Key Insights on Nearby Galaxies: a Far-Infrared Survey with *Herschel* (KINGFISH) sample of nearby galaxies (Dale et al. 2012). For this comparison, they only selected the normal galaxies in the KINGFISH sample using the spectral classification of Moustakas et al. (2010), and demonstrated that the BAT AGN FIR colours are statistically indistinguishable from those of normal galaxies. As our colour distribution for the total galaxies is compatible with the BAT AGN colour distribution, the colours of our galaxies are not statistically different from those of normal galaxies ($p = 0.20$) comparing our galaxies with normal galaxies in the KINGFISH sample (see also Table 9).

Shimizu et al. (2015) also studied the BAT sample and found anomalous colours for 6 BAT AGN with $f_\nu(250\ \mu m)/f_\nu(350\ \mu m) < 1.5$ and $f_\nu(350\ \mu m)/f_\nu(500\ \mu m) < 1.5$. They suggested that this might be an excess based on the synchrotron emission from the jet or the corona from the accretion disks. We do not find these anomalous colours for our galaxies.

We also compare the other integrated FIR colours of our galaxies with the KINGFISH sample of Dale et al. (2012) (including normal galaxies and AGN) and with the 85 nearby ($z \leqslant 0.5$) quasars from the Palomar-Green (PG) sample of Petric et al. (2015). In Fig. 6 we show the $f_\nu(100\ \mu m)/f_\nu(500\ \mu m)$ vs. $f_\nu(70\ \mu m)/f_\nu(250\ \mu m)$ colour-color diagram (left) and $f_\nu(250\ \mu m)/f_\nu(500\ \mu m)$ vs. $f_\nu(70\ \mu m)/f_\nu(160\ \mu m)$ colour-colour diagram (right) for our galaxies, the KINGFISH sample and the PG quasar sample. Most of the PG quasars only have upper limits of the fluxes for some bands. There are 65 quasars with upper limits at 500 μm, 29 at 250 μm, 16 at 160 μm, 4 at 100 μm and 2 at 70 μm. We do not display quasars with upper limits in the two fluxes involved in a ratio. In the left panel of Fig. 6 we show 81 quasars of the PG sample and in the right panel we show 54 quasars. We indicate with grey arrows the quasars with upper limits.

From Fig. 6, we observe that the $f_\nu(250\ \mu m)/f_\nu(500\ \mu m)$ and $f_\nu(70\ \mu m)/f_\nu(160\ \mu m)$ ratios of the RSA Seyfert galaxies (7.26 ± 1.21 and 0.78 ± 0.30, respectively) are, on average, higher than those of the KINGFISH sample (4.96 ± 1.73 and 0.63 ± 0.39, respectively). A K-S test indicates that the distributions of the two flux ratios are statistically different for our sample and the KINGFISH sample. We obtain p-values of $p = 0.002$ and $p = 10^{-7}$ for the $f_\nu(70\ \mu m)/f_\nu(160\ \mu m)$ and $f_\nu(250\ \mu m)/f_\nu(500\ \mu m)$ ratios, which indicates that they are statistically drawn from different parent samples. This may be due to the large range of morphologies and metallicities of the KINGFISH galaxies, whereas the RSA Seyfert galaxies are mostly early type (see Table 1). The differences in the integrated $f_\nu(70\ \mu m)/f_\nu(160\ \mu m)$ flux ratios are not in conflict with the comparison between the BAT AGN sample and the KINGFISH sample. Meléndez et al. (2014) compared their galaxies with the normal galaxies in the KINGFISH sample. A K-S test indicates that $f_\nu(70\ \mu m)/f_\nu(160\ \mu m)$ ratios of Meléndez et al. (2014) and all the KINGFISH sample are statistically different ($p = 0.003$).

4.3 Grey-body fitting

In this section we estimate the dust temperature by fitting the *Herschel* SED to a grey body. We use SHERPA (Doe et al. 2007), that is, the Chandra Interactive Analysis of Observations (*CIAO's*) *modelling and fitting package* (Freeman, Doe & Siemiginowska 2001) module for PYTHON. We fit νF_ν versus the rest-frame wavelength, using the following expression:

$$\nu F_{\nu_{model}} = \frac{A}{\lambda^{3+\beta}(e^{\frac{hc}{\lambda kT}} - 1)} \frac{c}{\lambda} \quad (1)$$

where λ is the rest-frame wavelength, and the free parameters of the fitting are the amplitude (A), the dust temperature (T), and the dust emissivity index (β). To estimate the best fit to the data we first minimized the usual χ^2 statistics leaving all the parameters to vary freely:

$$\chi^2 = \sum_i^N \frac{(\nu F_{\nu_i} - \nu F_{\nu_{i,model}})^2}{\sigma_i^2} \quad (2)$$

where N is the number of data points, F_{ν_i} is the flux at the ith wavelength, σ_i is the uncertainty of the observed flux at the ith wavelength, and $F_{\nu_{i,model}}$ is the predicted F_ν for the ith wavelength. We perform the fits for the integrated SEDs as well as for the nuclear $r = 1$ kpc and $r = 2$ kpc SEDs. We require four or more data points for the fittings.

Figure 7 shows a few examples of the best-fits to the SEDs for $r = 1$ kpc, $r = 2$ kpc, and the total galaxy. In the rest of the galaxies in the sample can be found in the online version. The values of the best-fit β and T parameters are listed in Table 10. Figure 8 shows the β distribution for each galaxy for $r = 1$ kpc, $r = 2$ kpc, and the total galaxy.

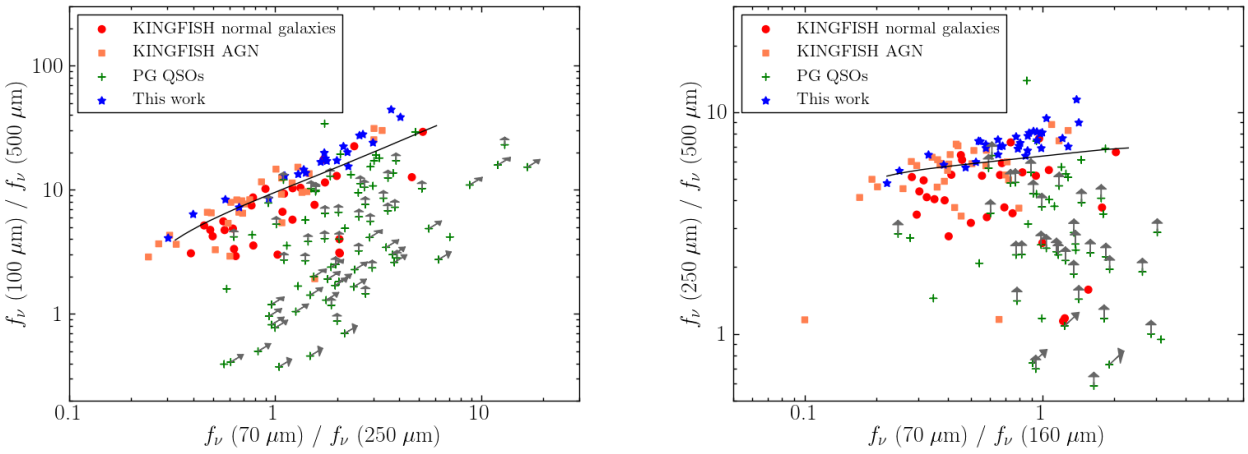

Figure 6. Colour-colour diagrams for our RSA Seyfert galaxies (blue stars), the normal galaxies from the KINGFISH sample (red circles) of Dale et al. (2012), the AGN galaxies from the KINGFISH sample (coral circles) and the PG quasar sample (green crosses) of Petric et al. (2015). The grey arrows are quasars with an upper limit to the flux. The solid lines indicate the models from Dale & Helou (2002). These models of SEDs are derived from the average global trends for a sample of normal star-forming galaxies.

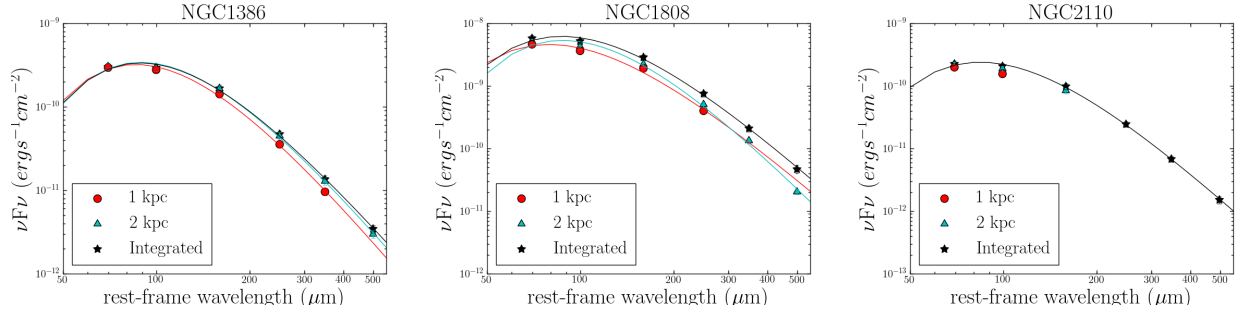

Figure 7. Examples of best fits to the FIR SEDs of the galaxies with a grey body with all the parameters left free to vary. The red circles are the fluxes for $r = 1$ kpc, the cyan triangles for $r = 2$ kpc and black stars for the total galaxy. The lines indicate the best fit in each region (only if there are 4 or more data points), with the colours as for the data points. The best fits for the rest of the galaxies can be found in the online version.

In Fig. 9 we show, for each galaxy, the dust temperature obtained in the fitting of the different regions (1 kpc, 2 kpc, the total galaxy). In Table 11 we provide the statistical information corresponding to Figs. 8 and 9. We show in parenthesis the total values for those 14 galaxies in our sample with SED fits within $r = 2$ kpc so we can compare the results for these galaxies in 2 kpc and the total galaxy.

For galaxies with SED fits in the three physical regions, we find that the nuclear regions with $r = 1$ kpc have the highest temperatures in agreement with the spatially resolved maps of the dust temperatures of Sánchez-Portal et al. (2013) for a few nearby Seyfert galaxies. The values obtained for the dust emissivity indices and temperatures for the integrated values are $1.0 < \beta < 2.0$ and $21 < T < 38$ K. These values of temperatures are in agreement with those obtained by Dale et al. (2012) ($18 < T < 40$ K) from fits to the $100 - 500\,\mu$m SEDs of KINGFISH galaxies. Our β values are also in agreement with the ones of Dale et al. (2012) ($1.2 < \beta < 1.9$). Pérez García, Rodríguez Espinosa, & Santolaya Rey (1998) studied 10 Seyfert galaxies observed with *ISO* and obtained that the MIR to FIR SEDs can be reproduced with three different components: warm, cold and very cold dust. Our temperature range is between the very cold component (T$\sim 10 - 20$ K) and the cold component (T$\sim 40 - 50$ K), so it may be due to dust heated by stars in the disc (cold component) and by the general interstellar radiation field of the galaxy (very cold component).

For some galaxies (e.g., NGC 3081, NGC 3783, and NGC 5347) the fit to the integrated SED does not reproduce well the 70 μm data point. We also tried fits to the integrated SEDs without this data point and found that for the majority of galaxies the reduced χ^2 values are higher with 70 μm data than without it. This suggests that in some galaxies this excess of 70 μm emission requires another component with a higher dust temperature, which could be associated with dust heated by the AGN. We will come back to this issue in Section 5.

To quantify the 70 μm excess in the integrated SED from the single temperature fits, we performed new grey body fits imposing β=2, which is the typical value for star forming galaxies (Li & Draine 2001). The statistical information about the fitted values of the dust temperature for

Table 10. Results from grey body fits. The full table is available in the online version.

Galaxy	emission in 1 kpc T	β	χ^2	emission in 2 kpc T	β	χ^2	Integrated emission T	β	χ^2	Integrated emission with β=2 T	χ^2	70 μm excess (%)
ESO323-G077							30±2	1.7±0.2	0.21	27.1±0.6	0.90	6
IC5063							38±4	1.0±0.2	2.82	25.9±0.8	6.99	59
Mrk1066							33±3	1.8±0.2	0.56	30.8±0.7	0.56	9
NGC1068				32±3	1.9±0.2	0.39	29±2	1.9±0.2	0.01	27.8±0.6	0.11	1
NGC1320							30±3	1.5±0.2	0.88	25.3±0.6	1.75	22

Table 11. Statistical information for the modified black body fits.

Quantity	Region	Number	Mean	σ	Median
Dust emissivity β	1 kpc	4	1.3	0.7	1.6
Dust emissivity β	2 kpc	15	1.9	0.4	1.8
Dust emissivity β	integrated	33 (15)	1.6 (1.6)	0.2 (0.2)	1.6 (1.5)
Reduced χ^2	1 kpc	4	1.47	1.34	0.77
Reduced χ^2	2 kpc	15	0.90	0.81	0.57
Reduced χ^2	integrated	33 (15)	0.76 (0.55)	0.66 (0.40)	0.65 (0.45)
Reduced χ^2, β=2	integrated	33 (15)	1.37 (1.23)	1.21 (0.73)	1.28 (1.28)
Dust temperature T(K)	1 kpc	4	33	7	31
Dust temperature T(K)	2 kpc	15	29	39	28
Dust temperature T(K)	integrated	33 (15)	28 (28)	3 (3)	29 (28)
Dust temperature T(K), β=2	integrated	33 (15)	25 (24)	3 (3)	26 (25)

Notes.— We show in parenthesis the total values for the 15 galaxies that also have SED fits within $r = 2$ kpc.

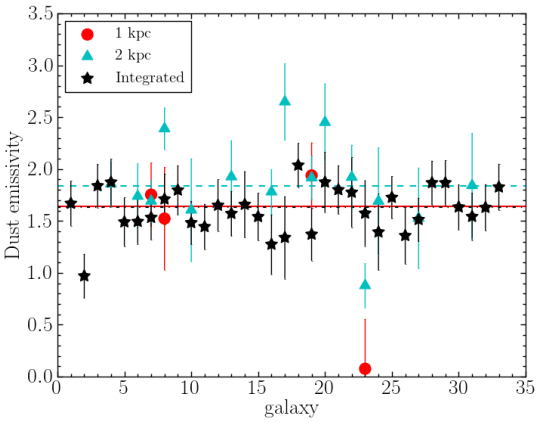

Figure 8. Distribution of the fitted dust emissivity indices β. For each galaxy, which is labelled on the horizontal axis with the number given in Table 1, we show β for $r = 1$ kpc (4 galaxies, red circles), $r = 2$ kpc (15 galaxies, cyan triangles), and the total galaxy (33 galaxies, black stars). The horizontal lines indicate the median values, red for $r = 1$ kpc, dashed cyan line for $r = 2$ kpc and the dash-dot black line for the total galaxy.

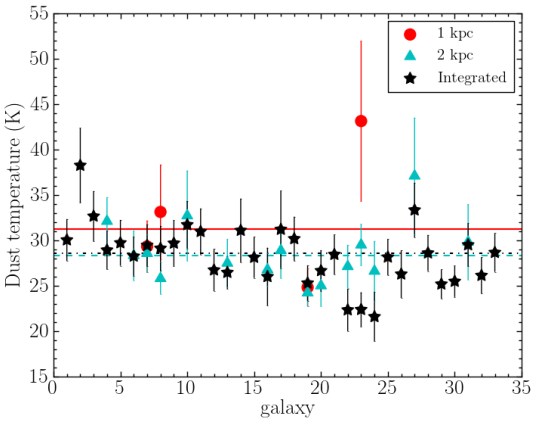

Figure 9. Dust temperature obtained through the grey body fitting for each galaxy labelled according to Table 1. We give the fitted temperature if available for $r = 1$ kpc (4 galaxies, red circles), $r = 2$ kpc (15 galaxies, cyan triangles), and the total galaxy (33 galaxies, black stars). The horizontal lines indicate the median values for $r = 1$ kpc (solid red line), $r = 2$ kpc (dashed cyan line) and total galaxy (dash-dot black line).

$\beta = 2$ are listed in Table 11. The range of dust temperatures obtained with the fit imposing β=2 is $18 - 31$ K, which are the normal temperatures for star forming galaxies. As expected, since β and T are anticorrelated (see e.g. Galametz et al. 2012, and also Figs. 8 and 9), for a given galaxy the fits with fixed dust emissivity $\beta = 2$ produce lower dust temperatures.

In Fig. 10 we show 4 RSA Seyfert galaxies with integrated SED fits with fixed dust emissivity $\beta = 2$ showing the highest excesses at 70 μm over the single temperature fits, which puts them clearly above the 1σ uncertainty of their fits. The data are shown in black, and the best fit with β=2 is shown in blue. The red lines indicate the best fit $\pm 1\sigma$ of the free parameters. The results for these fits for the rest of the sample are in the online version.

We quantify the excess over the fit at 70 μm as, $\frac{f_\nu(\mathrm{obs}) - f_\nu(\mathrm{model})}{f_\nu(\mathrm{model})}$, where f_ν(model) is the grey body fitted with $\beta = 2$ and free dust temperature and f_ν(obs) is the observed integrated value at 70 μm. In Table 10 we list in the last column the 70 μm excess. The average and median

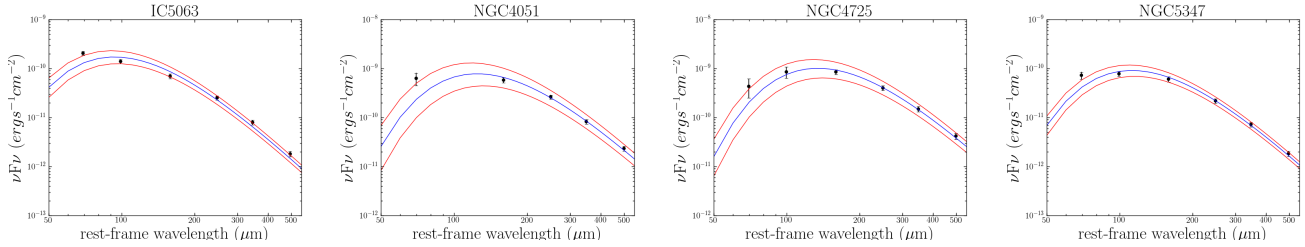

Figure 10. Fits to the integrated SEDs with β=2 for those RSA Seyfert galaxies with a clear excess over the fit at 70 μm. The blue line indicates the best fit, whereas the red lines delineate the best fit $\pm 1\sigma$ uncertainty. The fits for the rest of the RSA Seyferts in our sample are in the online version.

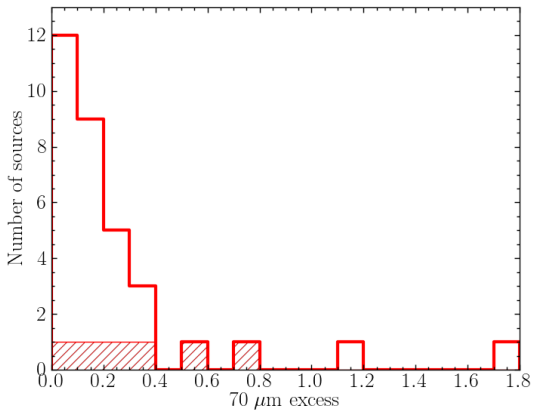

Figure 11. Distribution of the 70 μm integrated flux excesses calculated as $\frac{f_\nu(\mathrm{obs})-f_\nu(\mathrm{model})}{f_\nu(\mathrm{model})}$ (see Section 4.3). The hatched histogram shows the final sample of Seyferts with significant nuclear 70 μm AGN emission (see Section 5.6).

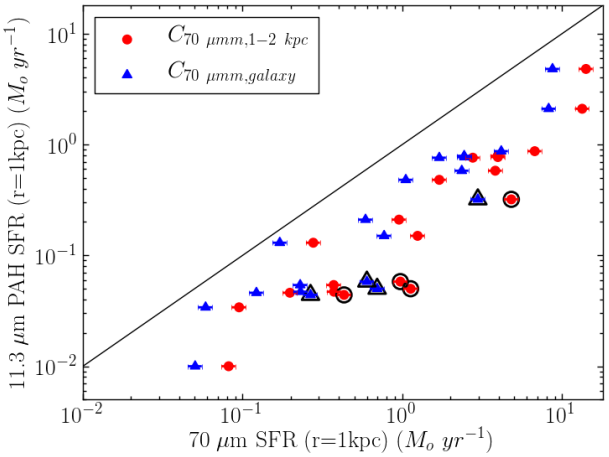

Figure 12. Nuclear SFR (r = 1 kpc) from the 70 μm luminosity versus the 11.3 μm PAH SFR (r = 1 kpc) from DSR2012. Red circles are the 70 μm-based SFR calculated with $C_{70\mu m,0.5-2kpc}$ = 0.94 (regions 0.5 − 2 kpc in size), whereas the blue triangles are SFR obtained with $C_{70\mu m,galaxy}$ = 0.58 (entire galaxy). The black line indicates the 1:1 relation. The 70 μm nuclear SFR uncertainties are derived by propagation of errors in the SFR formula, using the flux errors given in Tables 5, 6 and 7. The black symbols show the final selected Seyferts with significant nuclear 70 μm AGN emission (see Section 5.6). We note that there are two symbols for each galaxy, one for each coefficient.

70 μm excess of the sample are 26 per cent and 16 per cent, respectively, although some galaxies have high excesses, such as NGC 4051 (170 per cent excess) and NGC 4725 (114 per cent excess). In Fig. 11 we show the 70 μm excess distribution. We note that all the sources have a positive excess. These 70 μm excesses might be due to a hotter dust component not necessarily related to dust heated by an AGN (Galametz et al. 2012; Alonso-Herrero et al. 2012). We will discuss this further in Section 5.

4.4 Star Formation Rates

In this subsection we calculate the nuclear and extranuclear SFR using the 70 μm luminosity and compare them with the SFR obtained with other indicators. The goal is to identify galaxies where there is excess emission at 70 μm due to the AGN. We use the recipe from Li et al. (2013), which assumes a Kroupa (2001) IMF:

$$SFR(70\ \mu m)(M_\odot\ yr^{-1}) = C_{70\ \mu m,\mathrm{region}} \times 10^{-43} \times L(70\ \mu m)(erg\ s^{-1}) \quad (3)$$

The calibration coefficient $C_{70\ \mu m,\mathrm{region}}$ is different depending on the region of the galaxy. To calculate the SFR we used the coefficients from Calzetti et al. (2010) and Li et al. (2010), which are $C_{70\ \mu m,\mathrm{galaxy}}$ = 0.58 and $C_{70\ \mu m,0.5-2\ \mathrm{kpc}}$ = 0.94, respectively. The Calzetti et al. (2010) coefficient was derived from the integrated emission of galaxies and includes contributions from the diffuse component at 70 μm whereas the Li et al. (2010) measurements are local (star forming regions on scales of 0.5 − 2 kpc) and minimize the contribution of any diffuse component.

Figures 12 and 13 compare the values for the SFR obtained by DSR2012 with our 70 μm-based SFRs for the nuclear (r = 1 kpc) and extranuclear (r > 1 kpc) regions, respectively. We have 20 galaxies in common with DSR2012 with nuclear SFR values and 14 galaxies in common with the DSR2012 extranuclear SFR values. They obtained their nuclear SFR values from the luminosity of the 11.3 μm PAH feature and the extranuclear SFR from the luminosity of the extended 24 μm continuum emission after subtracting the contribution from the nuclear source. For the nuclear SFRs our values derived with the $C_{70\ \mu m,\mathrm{galaxy}}$ coefficient for the whole galaxy are on average four times higher than

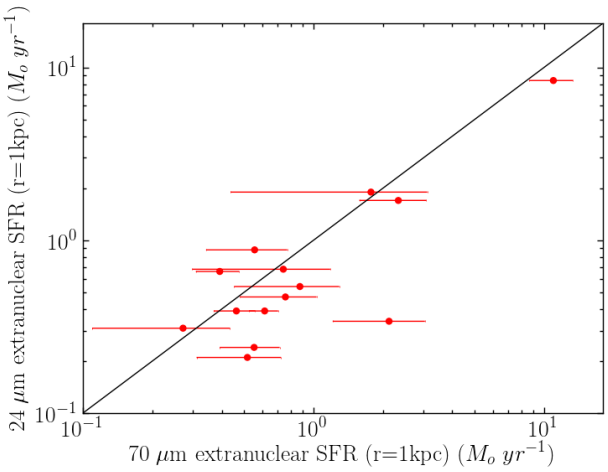

Figure 13. Extranuclear SFR ($r > 1$ kpc) estimated with the 70 μm-based SFR versus extranuclear ($r > 1$ kpc) 24 μm SFR from DSR2012. The black line indicates the 1:1 relation. The 70 μm extranuclear SFR uncertainties are calculated by propagation of errors in the SFR formula, using the flux errors given in Tables 5, 6 and 7.

those of DSR2012, and even a factor of 7 if we used the coefficient for $0.5 - 2$ kpc regions. These differences are larger than the quoted scatter of 0.14dex of the Li et al. (2010) calibration with some galaxies showing large discrepancies. For instance, NGC 3783 has a nuclear 70 μm based SFR 13.6 times higher than the nuclear 11.3 μm PAH based SFR. For the extranuclear SFRs, the majority of the galaxies in our sample have higher SFRs using the 70 μm emission than the DSR2012 value, although the galaxies appear to be closer to the 1:1 line.

The discrepancies in SFRs found for the RSA Seyferts are similar to those for the *Swift*/BAT AGN of Mushotzky et al. (2014). They calculated the total SFR using the Calzetti et al. (2010) 70 μm calibration, that is for the entire galaxy, and compared them with the SFR obtained from the 11.3 μm PAH feature using the calibration from DSR2012. They obtained a discrepancy of a factor of 3 between the two SFR. Petric et al. (2015) also found that the integrated galaxy SFRs of a sample of PG quasars obtained from the 11.3 μm PAH feature were on average 3 times lower than the SFR estimated from the $40 - 500$ μm emission.

All the differences in SFR described above could be explained if the carriers of the 11.3 μm PAH feature were being destroyed by the AGN radiation field, if there were aperture correction issues and/or if there were systematics in the calibrations. DSR2012 argued that SFR estimates using the 11.3 μm PAH feature appear to be robust to the effects of AGN and shock processing based on the good correlation with the [Ne II]12.8 μm line on kpc scales. Additionally Esquej et al. (2014) showed that even on smaller physical nuclear scales of nearby Seyferts there is no strong evidence for destruction of the 11.3 μm PAH carriers. The SFR differences do not seem to be due to the aperture corrections applied because all three works (DSR2012, Mushotzky et al. 2014 and Petric et al. 2015) also applied aperture corrections to their fluxes.

5 IDENTIFYING GALAXIES WITH SIGNIFICANT 70 μM EMISSION DUE TO AGN HEATED DUST

As the goal of this work is to select galaxies whose 70 μm emission is mostly due to dust heated by the AGN, in this section we put forward four different criteria to identify this type of galaxies. We also compare them with other results in the literature and propose candidate RSA galaxies with significant nuclear 70 μm AGN emission.

5.1 Elevated $f_\nu(70\,\mu\mathrm{m})/f_\nu(160\,\mu\mathrm{m})$ flux ratios

If the $f_\nu(70\,\mu\mathrm{m})/f_\nu(160\,\mu\mathrm{m})$ flux ratios are higher than the typical values for star forming galaxies, this might indicate that part of the nuclear 70 μm emission is due to the dust heated by the AGN instead of star formation. To select the galaxies with an elevated $f_\nu(70\,\mu\mathrm{m})/f_\nu(160\,\mu\mathrm{m})$ flux ratio we choose all the galaxies with a value higher than the median plus 1.4826 × M.A.D, where the M.A.D (absolute median deviation) is calculated as the median of the absolute deviations from the data median, M.A.D. = median($|x_i - \mathrm{median}_{\mathrm{data}}|$). We do this for the $r = 1$ kpc, $r = 2$ kpc, and integrated flux ratios using the statistics in Table 9, each one with its own value.

We select 9 galaxies with this criterion (see Table 12). We note that the 2 galaxies with high $f_\nu(70\,\mu\mathrm{m})/f_\nu(160\,\mu\mathrm{m})$ flux ratios within $r = 1$ kpc also show it within $r = 2$ kpc. All the galaxies with a high flux ratio within $r = 2$ kpc have high flux ratio at $r = 1$ kpc or have no measurements within 1 kpc. The same happens with the total flux ratio, galaxies with high total flux ratio have also high 2 kpc flux ratio or have no measurement at 2 kpc. However, not all galaxies with a high nuclear flux ratio have also high total flux ratio. Only NGC 5506 is selected from the flux ratios within $r = 2$ kpc and with the total galaxy flux. The rest have extended diffuse emission at 160 μm and therefore their measured integrated flux is higher at 160 μm than at 70 μm (see Fig. 2 and Table 7).

Figure 14 shows the relation between the $f_\nu(70\,\mu\mathrm{m})/f_\nu(160\,\mu\mathrm{m})$ flux ratio and the EW of the 6.2 and 11.3 μm PAH features measured from *Spitzer*/IRS spectra. The emission from these features is an indicator of the presence of on-going/recent star formation activity (Peeters et al. 2004) but can be diluted by the AGN continuum, resulting in lower EW (Spoon et al. 2007; Díaz-Santos et al. 2010; Hernán-Caballero & Hatziminaoglou 2011; Esquej et al. 2014). Note that not all the galaxies in our sample have a value of the EW (see Table 1). There is one galaxy that satisfies the criterion for $r = 2$ kpc without EW data.

As expected, those galaxies with a high value of the $f_\nu(70\,\mu\mathrm{m})/f_\nu(160\,\mu\mathrm{m})$ have a small value of the EW of the PAH features, indicating that it is a good criterion to select galaxies with the dust heated by the AGN. We note that the size of the IRS SL slit is similar to the FWHM at 70 μm. The only discrepant galaxy is the Seyfert 2 galaxy Mrk 1066, which has a high total $f_\nu(70\,\mu\mathrm{m})/f_\nu(160\,\mu\mathrm{m})$ flux ratio, but also a high value of the EW of the PAHs. Alonso-Herrero et al. (2014) and Ramos Almeida et al. (2014) have shown, based on high angular resolution (0.3arcsec) MIR spectroscopy, that this galaxy has a strong nuclear starburst

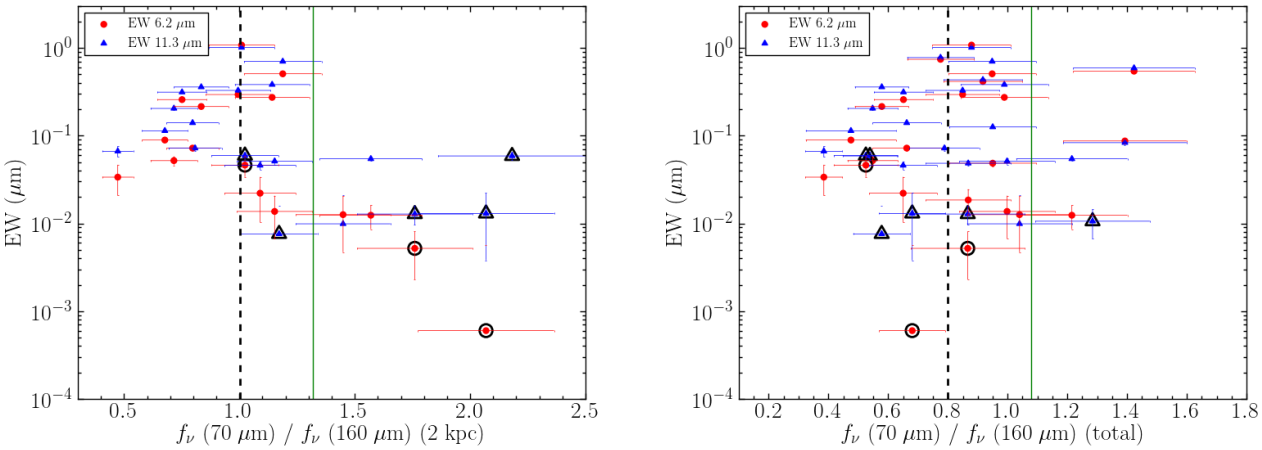

Figure 14. Relation between the $f_\nu(70\,\mu m)/f_\nu(160\,\mu m)$ flux ratio and the EW of the 6.2 μm (red circles) and 11.3 μm (blue triangles) PAH features as measured from *Spitzer*/IRS spectra. The left panel shows the relation for $r = 2$ kpc and the right panel for the total galaxy. The dashed black line indicates the median of each sample and the green line the median plus 1.4826 × M.A.D. The black symbols show the final selected Seyferts with significant nuclear 70 μm AGN emission (see Section 5.6).

including the central ~ 60 pc region. This would explain the elevated FIR colours of this galaxy. However, as can be seen from Fig. 14, not all galaxies with low PAH EWs features satisfy this criterion. Since the PAH features probe mostly the emission from O and B stars (Peeters et al. 2004), it is possible that some galaxies in our sample have most of their FIR emission mainly due to heating from older stars (see e.g. Li et al. 2010) explaining why they do not have bright PAH emission but still have normal FIR colours. Alternatively for these galaxies the torus emission might dominate in the MIR but it decays rapidly in the FIR (see Mullaney et al. 2011).

5.2 Dust temperature gradient higher than typical star forming galaxies

If the nuclear dust temperature is higher than those typical of star forming galaxies, this may indicate that the nuclear dust is not only heated by star forming but also by the AGN. However, because star-forming galaxies show a range of dust temperatures (Dale et al. 2012), for a given galaxy we compare the nuclear ($r = 1$ kpc and $r = 2$ kpc) temperatures to the dust temperature fitted for entire galaxy.

To select the galaxies with an elevated dust temperature gradient we use as criterion the ratio between the nuclear temperature and the total temperature for each galaxy. We select all the galaxies with a value higher than the median plus 1.4826 × M.A.D for our sample of galaxies. For this criterion we can use 15 galaxies, which are the galaxies with at least four data points to fit the $r = 2$ kpc SEDs. These 15 galaxies have similar mean integrated dust temperatures to those of the other RSA Seyfers (see Table 11). With this criterion we select 3 galaxies with higher dust temperature gradient than the typical in our sample. These are NGC 4579, NGC 4594, and NGC 4725.

5.3 Excess 70 μm emission with respect to the fit of the FIR SEDs with a grey body

The 70 μm excess with respect to the fit of the FIR SEDs with a grey body with β=2 could in principle indicate that this emission is not only due to star formation but that there is some contribution from the AGN. We select those galaxies whose excess at 70 μm is higher than the median plus 1.4826 × M.A.D for our sample of galaxies (28 per cent).

Figure 15 plots the 70 μm excess against the EW of the 6.2 and 11.3 μm PAH features as measured from the *Spitzer*/IRS spectra. Since those galaxies with a considerable excess also have small values of EW for both features, it is likely that this criterion selects galaxies with a contribution to the 70 μm from dust heated by the AGN. Again, as found for the FIR colours, not all galaxies with low EW of the PAH features have a 70 μm excess.

5.4 Excess of nuclear SFR obtained from 70 μm over SFR from mid-infrared indicators

As showed in Section 4.4, all the nuclear 70 μm-based SFR are systematically higher than those obtained by DSR2012 using the 11.3 μm PAH feature luminosity. We explained this as due to systematics in the calibrations. For this reason, we select those galaxies with the most discrepant values of SFR, i.e. all the galaxies with a value of SFR_{1kpc}/SFR_{D-S} higher than the median plus 1.4826 × M.A.D.. This could indicate that part of the nuclear 70 μm emission of these galaxies is due to the dust heated by the AGN. For this criterion we can use 20 galaxies that are the ones in common with DSR2012 and with measurements at 70 μm for $r = 1$ kpc. We select 4 galaxies with 70 μm-based nuclear SFR higher than expected taking into account the systematics in the calibrations, namely, NGC 3783, NGC 4151, NGC 7213, and NGC 7479. These four galaxies also satisfy some of the other criteria above.

Table 12. Summary of criteria to select galaxies with a significant AGN contribution at 70 μm.

Galaxy	#1 $f_\nu(70\,\mu m)/f_\nu(160\,\mu m)$			#2 $T_{region}/T_{Integrated}$		#3 70 μm	#4 $SFR_{70\mu m}/SFR_{D-S}$	criteria
	$r=1$ kpc	$r=2$ kpc	Integrated	$r=1$ kpc	$r=2$ kpc	excess	$r=1$ kpc	
ESO 323-G077	-	-	x	-	-	x	-	0/2
IC 5063	-	-	✓	-	-	✓	-	2/2
Mrk 1066	-	-	✓	-	-	x	-	1/2
NGC 1068	✓	✓	x	-	x	x	-	1/3
NGC 1320	-	x	x	-	-	x	-	0/2
NGC 1365	x	x	x	-	x	x	x	0/4
NGC 1386	x	x	x	x	x	x	x	0/4
NGC 1808	x	x	x	x	x	x	-	0/3
NGC 2110	-	x	x	-	-	x	-	0/2
NGC 2273	-	x	x	-	x	x	x	0/4
NGC 2992	-	x	x	-	-	x	x	0/3
NGC 3081	-	x	x	-	-	✓	x	1/3
NGC 3227	x	x	x	-	x	x	x	0/4
NGC 3281	-	✓	x	-	-	x	x	1/3
NGC 3783	-	✓	x	-	-	x	✓	2/3
NGC 4051	x	x	x	-	x	✓	x	1/4
NGC 4151	✓	✓	x	-	x	x	✓	2/4
NGC 4253	-	-	✓	-	-	x	-	1/2
NGC 4258	x	x	x	x	x	x	x	0/4
NGC 4388	-	x	x	-	x	x	x	0/4
NGC 4507	-	-	x	-	-	x	-	0/2
NGC 4579	x	x	x	-	✓	✓	x	2/4
NGC 4594	x	x	x	✓	✓	x	x	1/4
NGC 4725	-	x	x	-	✓	✓	x	2/4
NGC 5135	-	-	x	-	-	x	-	0/2
NGC 5347	-	x	x	-	-	✓	-	1/2
NGC 5506	-	✓	✓	-	x	x	x	1/4
NGC 7130	-	-	x	-	-	x	-	0/2
NGC 7172	-	x	x	-	-	x	x	0/3
NGC 7213	-	✓	x	-	-	x	✓	2/3
NGC 7465	-	x	x	-	x	x	-	0/3
NGC 7479	-	x	x	-	-	✓	✓	2/3
NGC 7582	x	x	x	-	-	x	x	0/3

Notes.— In bold are marked galaxies satisfying at least half of the conditions.

5.5 Comparison with other works

The results about the nuclear 70 μm emission obtained with the above criteria are in good agreement with the detailed *Herschel* imaging studies of the infrared emission of three Seyfert galaxies, NGC 1365, NGC 2992, and NGC 3081 mentioned in Section 1. Alonso-Herrero et al. (2012) and García-Bernete et al. (2015) found that the AGN emission does not dominate the 70 μm emission of NGC 1365 and NGC 2992, respectively. These two galaxies do not satisfy any of our selection criteria. On the other hand, Ramos Almeida et al. (2011) assumed that the nuclear 70μm flux of NGC 3081 is due to dust heated in the torus surrounding the AGN. They modelled the unresolved infrared emission of this galaxy with the Nenkova et al. (2008) clumpy torus models and were able to reproduce the AGN bolometric luminosity. This galaxy satisfies the 70 μm excess emission with respect to the fit of the FIR SEDs with a grey body with $\beta = 2$ criterion. The reason why this galaxy does not meet the other criteria may be due to the nuclear ring of 2 kpc in diameter. Because of its distance we were not able to derive nuclear $r = 1$ kpc dust temperature and $f_\nu(70\,\mu m)/f_\nu(160\,\mu m)$ flux ratio. Therefore we were restricted to measurements within $r = 2$ kpc and the total galaxy.

We have 4 galaxies in common with the work of Mullaney et al. (2011), namely, NGC 2110, NGC 4507, NGC 5506, and IC 5063. Among these they found that the only galaxy dominated by the AGN emission at 60 μm is IC 5063 in good agreement with our results.

5.6 Inspection of the candidates to significant nuclear 70 μm AGN emission

Table 12 summarizes the selection criteria fulfilled by each galaxy. In the last column we indicate the number of criteria satisfied by each galaxy. 16 galaxies (48 per cent of the sample) satisfy at least one of these requirements, while 10 of them fit at least half of the criteria. We found no differences between Seyfert 1 and 2 in terms of the selection requirements (p=0.30 with the Fisher's test). Of the 16 galaxies that satisfy at least one criterion, 9 are Seyfert 1 and 7 Seyfert 2. We also found no differences between the galaxies that satisfy at least one criterion and the galaxies that donot satisfy any of them in terms of AGN luminosity or 70 μm luminosity.

In what follows we take a conservative approach by only considering the 10 RSA Seyferts in our sample that satisfy

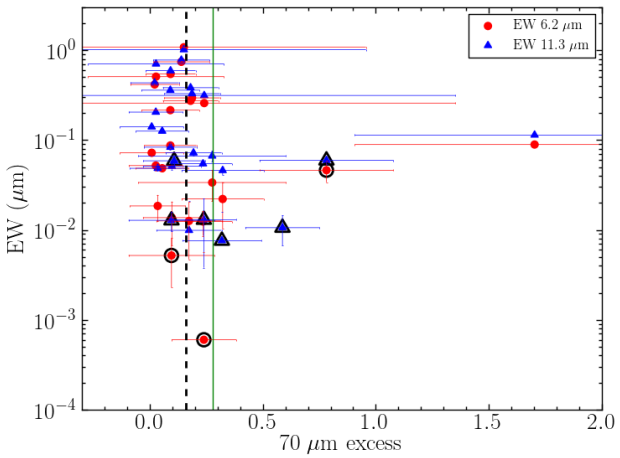

Figure 15. Relation between the 70 μm excess and the EW of the 6.2 μm (red circles) and 11.3 μm (blue triangles) PAH features as measured from *Spitzer*/IRS spectra. The dashed black line indicates the median of each sample and the green line the median plus 1.4826 × M.A.D. The black symbols show the final selected Seyferts with significant nuclear 70 μm AGN emission (see Section 5.6).

half or more of the criteria defined in the previous sections to select candidates with a significant AGN contribution to the nuclear 70 μm emission.

We start by discarding two galaxies, NGC 4253 and Mrk 1066, as both show 11.3 μm PAH emission in the inner 0.5 arcseconds, equivalent to physical sizes of 120 and 145 pc, respectively (Alonso-Herrero et al. 2014, 2016) as well as high SFR within $r = 1$ kpc scales. This probably suggests that the elevated $f_\nu(70\,\mu\mathrm{m})/f_\nu(160\,\mu\mathrm{m})$ flux ratios are due to strong star formation rather than AGN dominated fluxes at 70 μm (see Ramos Almeida et al. 2014, for a detailed discussion of Mrk 1066).

We next discuss NGC 4579 and NGC 4725, which are among the least luminous AGN in our sample of RSA Seyferts. Both are close to the low-luminosity AGN (LLAGN) limit of 10^{42} erg s^{-1} below which the dusty torus is predicted to disappear (Elitzur & Shlosman 2006). As can be seen from Table 10, both galaxies show a significant excess at 70 μm with respect to the $\beta = 2$ grey body fit to the integrated SED. However, if we assumed that the excess is entirely due to dust heated by the AGN, then the AGN flux at 70 μm would be similar to the measured nuclear $r = 1$ kpc flux for NGC 4579 which is resolved (FWHM=600 pc) at this wavelength. For NGC 4725 the predicted AGN flux would be more than twenty times brighter than that arising from the nuclear (resolved) region with a 1.4 kpc size (FWHM). We therefore conclude that the 70 μm nuclear emission of NGC 4579 and NGC 4725 at the *Herschel* resolution is not dominated by dust heated from the AGN.

We are left with six (18 per cent of the sample) *bona fide* candidates, namely, IC 5063, NGC 3783, NGC 4151, NGC 5347, NGC 7213, and NGC 7479.

5.7 MIR and FIR emission of the candidates to significant nuclear 70 μm AGN emission

None of the six candidates shows 11.3 μm PAH emission in high angular resolution (0.5-0.7 arcsec scales) MIR spectroscopy (Alonso-Herrero et al. 2011; González-Martín et al. 2013; Esquej et al. 2014; Alonso-Herrero et al. 2016) and all of them show low values of the nuclear SFRs (see Table 1). Hernán-Caballero et al. (2015) performed a spectral decomposition of 118 *Spitzer* IRS spectra of local AGN. The 6 candidates have a high AGN contribution (within the IRS slit) at $\lambda < 15\,\mu$m and an AGN 12 μm luminosity in agreement with the estimates from nuclear high angular resolution spectra (Alonso-Herrero et al. 2011; González-Martín et al. 2013). We show the selected galaxies as the hatched histogram in Fig. 11 and with black symbols in Figs. 12, 14, and 15.

We used the different criteria to estimate the range of the AGN flux at 70 μm. For each galaxy we only used the criteria satisfied (see Table 12). For the galaxies that have a 70 μm excess with respect to the fit of the FIR SEDs with a $\beta = 2$ grey body (see Section 5.3), we can estimate directly the AGN flux. For the galaxies that satisfied the elevated $f_\nu(70\,\mu\mathrm{m})/f_\nu(160\,\mu\mathrm{m})$ flux ratios (see Section 5.1), or the excess of nuclear SFR obtained from 70 μm over SFR from mid-infrared indicators (see Section 5.4) we make the observed values compatible with the typical values of the sample, and the excess is assumed to be the AGN emission. For IC 5063 we obtain an AGN flux at 70 μm of 1.8 Jy (40 per cent of the nuclear r = 2 kpc flux) using the two criteria. For NGC 5347 we can only calculate the contribution with the excess with respect to the $\beta = 2$ grey body fit. The AGN contribution is approximately 0.7 Jy (61 per cent of the nuclear r = 1 kpc flux). For the rest of the galaxies we obtain different fluxes depending on the criterion used to estimate the 70 μm AGN flux. The ranges are $1.0 - 1.3$ Jy for NGC 3783 ($56 - 73$ per cent of the nuclear r = 1 kpc flux); $2.4 - 3.0$ Jy for NGC 4151 ($49 - 62$ per cent of the nuclear r = 1 kpc flux); $0.5 - 1.1$ Jy for NGC 7213 ($35 - 76$ per cent of the nuclear r = 1 kpc flux); and $4.1 - 5.4$ Jy for NGC 7479 ($43-57$ per cent of the nuclear r = 1 kpc flux). We finally note that the estimated AGN 70 μm fluxes for IC 5063 and NGC 4151 are in good agreement with the predicted torus FIR emission from the extrapolation of the fits to the unresolved near-infrared and MIR emission (Alonso-Herrero et al. 2011; Ichikawa et al. 2015) using clumpy torus models.

Figure 16 shows the *Spitzer*/IRS SL+LL spectra for these six galaxies, normalized at 30 μm. We also plot the estimated AGN 70 μm flux ranges and the average SEDs of the low luminosity ($\log(\frac{L_{2-10keV}}{\mathrm{erg\,s^{-1}}}) < 42.9$) and high luminosity ($\log(\frac{L_{2-10keV}}{\mathrm{erg\,s^{-1}}}) > 42.9$) AGN of Mullaney et al. (2011), all of them normalized at 30 μm. All our candidates have MIR and 70 μm AGN emission entirely consistent with the empirically determined low and high luminosity AGN templates of Mullaney et al. (2011), except around the 9.7 μm silicate feature range for the two most extreme features (NGC 7213 and NGC 7479).

In summary, for our sample of 33 RSA Seyferts we found a small fraction of galaxies (6/33, 18 per cent) with a significant contribution from AGN heated dust to the nuclear 70 μm emission. This fraction is similar to the findings of Mullaney et al. (2011) for a sample of X-ray selected sample

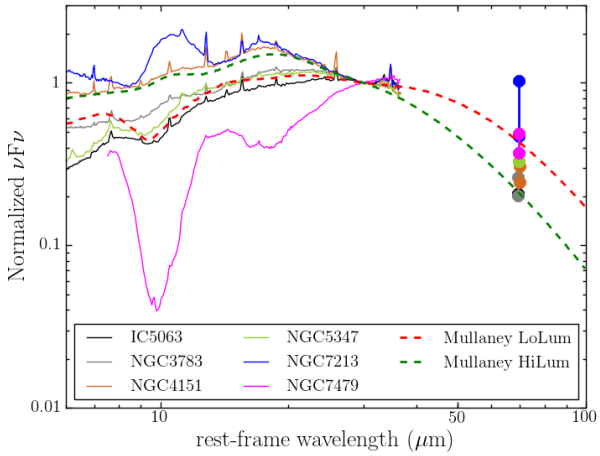

Figure 16. *Spitzer*/IRS SL+LL spectra normalized at 30 μm of the six candidates to significant nuclear 70 μm AGN emission. The estimated AGN 70 μm flux ranges (see Section 5.6) are shown with filled circles, normalized to the IRS flux at 30 μm for each galaxy. The red and green dashed lines indicate, respectively, the average SED of the empirically determined low luminosity ($\log(\frac{L_{2-10keV}}{\mathrm{erg\,s^{-1}}}) < 42.9$) and high luminosity ($\log(\frac{L_{2-10keV}}{\mathrm{erg\,s^{-1}}}) > 42.9$) AGN of Mullaney et al. (2011), also normalized at 30 μm.

with no evidence of host emission in their MIR *Spitzer*/IRS spectra. They only identified 4 galaxies out of the 25 AGN with FIR emission dominated by the AGN. This demonstrates that our FIR method to select galaxies with significant nuclear 70 μm AGN emission for optically selected Seyferts produces similar results to their MIR based method for X-ray selected AGN.

6 SUMMARY AND CONCLUSIONS

In this work we studied the nuclear and integrated FIR ($70 - 500\,\mu$m) emission of 33 nearby (median distance of 30 Mpc) Seyfert galaxies from the RSA catalogue using *Herschel*/PACS and SPIRE imaging observations. We selected these galaxies because they are nearby and have estimates of their nuclear and integrated SFR. The goal was to identify galaxies with a significant fraction of their 70 μm emission produced by dust heated by the AGN by taking advantage of the broad FIR spectral coverage and the good angular resolution at 70 μm (median 0.8 kpc FWHM for our sample). We analysed the FIR properties of our sample, such as the unresolved 70 μm emission and the nuclear ($r = 1$ kpc and $r = 2$ kpc) and integrated FIR colours. We fitted grey-bodies to their SEDs and derived nuclear and integrated SFR. We finally put forward four criteria to select galaxies whose nuclear 70 μm emission has a significant AGN contribution. These were: (1) elevated $f_\nu(70\,\mu\mathrm{m})/f_\nu(160\,\mu\mathrm{m})$) flux ratios to the typical colours of star forming galaxies, (2) dust temperature gradient higher than typical values of star forming galaxies, (3) 70 μm excess emission with respect to the fit of the integrated FIR SEDs with a grey body with a fixed dust emissivity $\beta = 2$, and (4) excess of nuclear SFR obtained from 70 μm over SFR from mid-infrared indicators. The main results are as follows.

- At 70 μm most RSA Seyfert galaxies (85 per cent) in our sample have a nuclear $r = 2$ kpc contribution to the total flux greater than 50 per cent. This is in good agreement with results for the *Swift*/BAT AGN sample of Mushotzky et al. (2014). The derived 70 μm sizes (FWHM) indicate that a significant fraction of this emission arises from regions $0.3 - 2$ kpc in size.
- The nuclear $f_\nu(70\ \mu m)/f_\nu(160\ \mu m)$ flux ratio is higher in the nuclear regions than for the entire galaxy. The integrated $f_\nu(70\ \mu m)/f_\nu(160\ \mu m)$ flux ratio distribution is statistically indistinguishable from the distribution of the *Swift*/BAT AGN sample of Meléndez et al. (2014) and from the normal galaxies of the KINGFISH sample Dale et al. (2012). This confirms previous results that the integrated FIR emission of Seyfert galaxies is in general dominated by the emission from their host galaxies rather than from the AGN.
- The grey body fits to the nuclear regions and the total galaxy SEDs show that for a given galaxy the nuclear regions ($r = 1$ kpc) have the highest temperatures, in agreement with the spatially resolved maps of the dust temperatures of nearby Seyfert and normal galaxies (see e.g. Bendo et al. 2012; Sánchez-Portal et al. 2013). The fitted dust temperatures ($21 < T < 38$ K) and dust emissivities ($1.0 < \beta < 2.0$) from the integrated SEDs are similar to those of normal galaxies.
- When fitting the integrated SEDs using β=2, which is the typical value for star forming galaxies (Li & Draine 2001), we found that 7 Seyfert galaxies in our sample have a 70 μm excess over the fit greater than 28 per cent. This suggests the presence of a hotter dust component, which could be associated to the presence of a nuclear starburst and/or dust heated by the AGN.
- The 70 μm nuclear SFRs derived with the $C_{70\mu\mathrm{m,galaxy}}$ coefficient are on average 4 times higher than those obtained by DSR2012 using the 11.3 μm PAH feature. Mushotzky et al. (2014) and Petric et al. (2015) also found a discrepancy of 3 between the SFR calculated through 70 μm and through 11.3 μm PAH feature.
- Taking into account the four criteria defined to select galaxies whose nuclear 70 μm emission has a significant AGN contribution, we found that 16 galaxies (48 per cent of the sample) satisfy at least one of these criteria, whereas 10 satisfy half or more of the criteria.
- By careful examination of the 10 candidates satisfying at least half of the criteria, we selected six RSA Seyfert galaxies (18 per cent of the initial sample) whose nuclear ($r = 1 - 2$ kpc) 70 μm emission has a significant ($\sim 40 - 70$ per cent) contribution from dust heated by the AGN. These galaxies are IC 5063, NGC 3783, NGC 4151, NGC 5347, NGC 7213, and NGC 7479. Four of them are Sy1 and 2 of them are Sy2. None of them show 11.3 μm PAH emission on scales of tens of parsecs from high angular resolution MIR spectroscopy or high nuclear SFR.
- Our FIR method to select galaxies whose nuclear 70 μm emission has a significant AGN contribution for optically selected Seyferts produces similar results to the Mullaney et al. (2011) MIR based method for X-ray selected AGN, in

terms of the fraction of galaxies dominated by the AGN at 70 μm and the spectral shapes between 5 and 70 μm.

The criteria defined in this work provide a good way to select statistically Seyferts with significant contribution of the AGN at 70 μm using Herschel data.

Acknowledgements

We thank the referee for valuable comments that helped improve the paper.

J.G.-G. acknowledges financial support from the Universidad de Cantabria through the Programa de Personal Investigador en Formación Predoctoral de la Universidad de Cantabria. J.G.-G., A.A.-H. and A.H.-C. acknowledge financial support from the Spanish Ministry of Economy and Competitiveness through grant AYA2012-31447, which is party funded by the FEDER program. P.E. acknowledges support from the Spanish Programa Nacional de Astronomía y Astrofísica under grant AYA2012-31277. C.R.-A. is supported by a Marie Curie Intra European Fellowship within the 7th European Community Framework Programme (PIEF-GA- 2012-327934). T.D.-S. acknowledges support from ALMA-CONICYT project 31130005 and FONDECYT project 1151239. J.G.-G. thanks A. Khan-Ali for his support and help with SHERPA. J.G.-G. also thanks A. Marcos-Caballero for his comments on statistics. The authors also thank E. Hatziminaoglou for her insightful comments.

Based on observations made with *Herschel*, which is an ESA space observatory with science instruments provided by European-led Principal Investigator consortia and with important participation from NASA. PACS has been developed by a consortium of institutes led by MPE (Germany) and including UVIE (Austria); KU Leuven, CSL, IMEC (Belgium); CEA, LAM (France); MPIA (Germany); INAF-IFSI/OAA/OAP/OAT, LENS, SISSA (Italy); IAC (Spain). This development has been supported by the funding agencies BMVIT (Austria), ESA-PRODEX (Belgium), CEA/CNES (France), DLR (Germany), ASI/INAF (Italy), and CICYT/MCYT (Spain).SPIRE has been developed by a consortium of institutes led by Cardiff University (UK) and including Univ. Lethbridge (Canada); NAOC (China); CEA, LAM (France); IFSI, Univ. Padua (Italy); IAC (Spain); Stockholm Observatory (Sweden); Imperial College London, RAL, UCL-MSSL, UKATC, Univ. Sussex (UK); and Caltech, JPL, NHSC, Univ. Colorado (USA). This development has been supported by national funding agencies: CSA (Canada); NAOC (China); CEA, CNES, CNRS (France); ASI (Italy); MCINN (Spain); SNSB (Sweden); STFC, UKSA (UK); and NASA (USA).

HIPE is a joint development by the Herschel Science Ground Segment Consortium, consisting of ESA, the NASA Herschel Science Center, and the HIFI, PACS and SPIRE consortia.

This research has made use of the NASA/IPAC Extragalactic Database (NED) which is operated by the Jet Propulsion Laboratory, California Institute of Technology, under contract with the National Aeronautics and Space Administration.

This research has made use of the TOPCAT software (http://www.starlink.ac.uk/topcat/) and its tools.

REFERENCES

Alonso-Herrero A., et al., 2011, ApJ, 736, 82
Alonso-Herrero A., et al., 2012, MNRAS, 425, 311
Alonso-Herrero A. et al. 2014, MNRAS, 443, 2766
Alonso-Herrero A., et al., 2016, MNRAS, 455, 563
Antonucci R., 1993, ARA&A, 31, 473
Bendo G. J., et al., 2012, MNRAS, 419, 1833
Bradt H. V., Burke B. F., Canizares C. R., Greenfield P. E., Kelley R. L., McClintock J. E., van Paradijs J., Koski A. T., 1978, ApJ, 226, L111
Brightman M., Nandra K., 2011, MNRAS, 413, 1206
Calzetti D. et al., 2010, ApJ, 714, 1256
Contini T., Considere S., Davoust E., 1998, A&AS, 130, 285
Dale D. A., et al., 2012, ApJ, 745, 95
Dale D. A., Helou G., 2002, ApJ, 576, 159
de Vaucouleurs G., de Vaucouleurs A., Corwin H. G., Jr., Buta R. J., Paturel G., Fouque P., 1991, S&T, 82, 621
Diamond-Stanic A. M., Rieke G. H., 2010, ApJ, 724, 140
Diamond-Stanic A. M., Rieke G. H., 2012, ApJ, 746, 168
Díaz-Santos T., Alonso-Herrero A., Colina L., Packham C., Levenson N. A., Pereira-Santaella M., Roche P. F., Telesco C. M., 2010, ApJ, 711, 328
Doe S. et al., 2007, Astronomical Data Analysis Software ans Systems XVI, 376, 543
Esquej P., Alonso-Herrero A., González-Martín O., Hönig S., Hernán-Caballero A., et al., 2014, ApJ, 780, 86
Elitzur M., Shlosman I. 2006, ApJ, 648, L101
Freeman P. E., Doe S., Siemiginowska A., 2001, SPIE Proceedings, Vol. 4477, p. 76
Fritz J., Franceschini A., Hatziminaoglou E., 2006, MNRAS, 366, 767
Galametz M. et al. 2012, MNRAS, 425, 763
García-Bernete I., et al., 2015, MNRAS, 449, 1309
González-Martín O., et al., 2013, A&A, 553, A35
González-Martín O., et al., 2015, A&A, 578, A74
Griffin, M.J. et al., 2010, A&A, 518, 3
Hatziminaoglou E., et al., 2010, A&A, 518, L33
Healey S. E., Romani R. W., Taylor G. B., Sadler E. M., Ricci R., Murphy T., Ulvestad J. S., Winn J. N., 2007, ApJS, 171, 61
Hernán-Caballero A., Hatziminaoglou E. 2011, MNRAS, 414, 500
Hernán-Caballero A., et al., 2015, ApJ, 803, 109
Hernán-Caballero A., Spoon H. W. W., Lebouteiller V., Rupke D. S. N., Barry D. P., 2016, MNRAS, 455, 1796
Hönig S. F., Kishimoto M., 2010, A&A, 523, A27
Hönig S., et al., 2010, A&A, 515, 23
Kewley L. J., Heisler C. A., Dopita M. A., Lumsden S., 2001, ApJS, 132, 37
Ichikawa K., et al., 2015, ApJ, 803, 57
Khachikian E. Y., Weedman D. W., 1974, ApJ, 192, 581
Kroupa P., 2001, MNRAS, 322, 231
Lebouteiller V., Barry D. J., Spoon H. W. W., et al., 2011, ApJS, 196, 8
Lebouteiller V., Barry D. J., Goes C., Sloan G. C., Spoon H. W. W., Weedman D. W., Bernard-Salas J., Houck J. R., 2015, ApJS, 218, 21
Li Y., Calzetti D., Kennicutt R. C., Hong S., Engelbracht C. W., Dale D. A., Moustakas J., 2010, ApJ, 725, 677
Li A., Draine B. T., 2001, ApJ, 554, 778
Li Y. et al., 2013, ApJ, 768, 180
Maiolino R., Rieke G. H., 1995, ApJ, 454, 95
Malizia A., Bassani L., Bazzano A., Bird A. J., Masetti N., Panessa F., Stephen J. B., Ubertini P., 2012, MNRAS, 426, 1750
Mason R. E. et al. 2012, AJ, 144, 11
Meléndez M., Mushotzky R. F., Shimizu T. T., Barger A. J., Cowie L. L., 2014, ApJ, 794, 152

Moustakas J., Kennicutt Jr., R. C., Tremonti C. A., Dale D. A., Smith J.-D. T., Calzetti D. 2010, ApJS, 190, 233
Mullaney J., Alexander D. M., Goulding A. D., Hickox R. C. 2011, MNRAS, 414, 1082
Mushotzky R. F., Shimizu T. T., Meléndez M., Koss M., 2014, ApJL, 781, 34
Nenkova M., Sirocky M. M., Nikutta R., Ivezić Z., Elitzur M., 2008, ApJ, 685, 160
Osterbrock D. E., Martel A., 1993, ApJ, 414, 552
Ott S., 2010, ASP Conference Series, 434, 139
Panessa F., Bassani L., 2002, A&A, 394, 435
Peeters E., Spoon H. W. W., Tielens A. G. G. M. 2004, ApJ, 613, 986
Pérez García A. M., Rodríguez Espinosa J. M., Santolaya Rey A. E., 1998, ApJ, 500, 685
Petric A. O., Ho L. C., Flagey N. J. M., Scoville N. Z., 2015, ApJS, 219, 22
Phillips M. M., Charles P. A., Baldwin J. A., 1983, ApJ, 266, 485
Poglitsch A. et al., 2010, A&A, 518, 2
Ramos Almeida C., et al., 2011, MNRAS, 417, L46
Ramos Almeida C. et al. 2014, MNRAS, 445, 1130
Reunanen J., Kotilainen J. K., Prieto M. A., 2002, MNRAS, 331, 154
Rieke G. H., 1978, ApJ, 226, 550
Rodríguez Espinosa J. M., Rudy R. J., Jones B., 1987, ApJ, 312, 555
Roussel H., 2013, PASP, 125, 1126
Sánchez-Portal, M. et al. 2013, in Highlights of Spanish Astrophysics VII, Proceedings of the X Scientific Meeting of the Spanish Astronomical Society (SEA), held in Valencia, July 9 - 13, 2012, Eds.: J.C. Guirado, L.M. Lara, V. Quilis, and J. Gorgas., pp.392-398
Sandage A., Tammann G. A., 1987, A revised Shapley-Ames Catalog of bright galaxies (2nd ed.; Washington, DC: Carnegie Institution of Washington)
Shimizu T. T., Melendez M., Mushotzky R. F., Koss M. J., Barger A. J., Cowie L. L., 2015, arXiv, arXiv:1512.02733
Skibba, R. A., et al. 2011, ApJ, 738, 89
Spinoglio L., Andreani P., Malkan M. A. 2002, ApJ, 572, 105
Spoon H. W. W., Marshall J. A., Houck J. R., Elitzur M., Hao L., Armus L., Brandl B. R., Charmandaris V., 2007, ApJ, 654, L49
Trippe M. L., Crenshaw D. M., Deo R. P., Dietrich M., Kraemer S. B., Rafter S. E., Turner T. J., 2010, ApJ, 725, 1749
Véron-Cetty M. P., Véron P., 2006, A&A, 455, 773

This paper has been typeset from a TEX/LATEX file prepared by the author.